High-order fluid solver based on a combined compact integrated RBF approximation and its fluid structure interaction applications

C.M.T. Tien[a], D. Ngo-Cong[a], N. Mai-Duy[a], C.-D. Tran[a], T. Tran-Cong[a,*]

[a] *Computational Engineering and Science Research Centre, Faculty of Health, Engineering and Sciences, The University of Southern Queensland, Toowoomba, Queensland 4350, Australia.*

Abstract

In this study, we present a high-order numerical method based on a combined compact integrated RBF (IRBF) approximation for viscous flow and fluid structure interaction (FSI) problems. In the method, the fluid variables are locally approximated by using the combined compact IRBF, and the incompressible Navier-Stokes equations are solved by using the velocity-pressure formulation in a direct fully coupled approach. The fluid solver is verified through various problems including heat, Burgers, convection-diffusion equations, Taylor-Green vortex and lid driven cavity flows. It is then applied to simulate some FSI problems in which an elastic structure is immersed in a viscous incompressible fluid. For FSI simulations, we employ the immersed boundary framework using a regular Eulerian computational grid for the fluid mechanics together with a Lagrangian representation of the immersed boundary. For the immersed fibre/membrane FSI problems, although the or-

*Corresponding author

Email address: thanh.tran-cong@usq.edu.au (T. Tran-Cong)

der of accuracy of the present scheme is generally similar to FDM approaches reported in the literature, the present approach is nonetheless more accurate than FDM approaches at comparable grid spacings. The numerical results obtained by the present scheme are highly accurate or in good agreement with those reported in earlier studies of the same problems.

Keywords:

Combined compact integrated RBF; Convection-diffusion equations; Fluid flow; Fluid structure interaction; Enclosed membrane; Immersed boundary.

---

1. Introduction

Although many scientific and engineering problems involve fluid structure interaction (FSI), thorough study of such problems remains a challenge due to their strong nonlinearity and multidisciplinary requirements [1, 2, 3]. For most FSI problems, closed form analytic methods to the model equations are often not available, while laboratory experiments are not practical due to limited resources. Therefore, to investigate the fundamental physics involved in the complicated interaction between fluids and solids, one has to rely on numerical methods [4].

In this study, we are interested in the interaction of a viscous incompressible fluid with an immersed elastic membrane. The immersed boundary method (IBM), originally developed by Peskin [5], is designed to solve this kind of problem. The IBM is a mixed Eulerian-Lagrangian scheme in which the fluid dynamics based on the Navier-Stokes (N-S) equations are described in Eulerian form, and the elasticity of the structure is described in Lagrangian form. The IBM considers the structure as an immersed boundary which can be represented by a singular force in the N-S equations rather than a real body. It avoids grid-conforming difficulties associated with the moving boundary faced by conventional body-fitted methods. The fluid computation is done on a fixed, uniform computational lattice and the representation of the immersed boundary is independent of this lattice. The immersed boundary exerts a singular force on the nearby lattice points of the fluid with the help of a computational model of the Dirac δ-function. At the same time, the representative material points of the immersed boundary move at the local fluid velocity, which is obtained by interpolation from the nearby lattice points of the fluid. The same δ-function weights are used in the interpolation step as in the application of the boundary forces on the fluid. Computer simulations using the IBM such as blood flow in the heart [5, 6], insect flight [7], aquatic animal locomotion [8], bio-film processing [9], and flow past a pick-up truck [10] have exhibited the great potential of the IBM in FSI applications. Reviews on immersed methods can be found in [11, 12].

High-order approximation schemes have the ability to produce highly accurate solutions to incompressible viscous flow problems. With these schemes, a high level of accuracy can be achieved using a relatively coarse discretisation. Many types of high-order approximation methods have been reported in the literature. Botella and Peyret [13] developed a Chebyshev collocation method for the lid-driven cavity flow. Various types of high-order compact finite difference algorithms (HOC) were proposed [14, 15, 16]. On the other hand, radial basis function networks (RBF) have emerged as a powerful approximation tool [17, 18, 19]. Different schemes of integrated RBF approximation (here referred to as IRBF) were developed in the literature [20, 21, 22, 23]. In [24], the authors developed a high-order fully coupled scheme based on compact IRBF approximations for viscous flow problems, where nodal first- and second-derivative values are included in the stencil approximation and the starting points in the integration process are second-order derivatives. In their work, the N-S governing equations are taken in the primitive form where the velocity and pressure fields are solved in a direct fully coupled approach. With relatively coarse meshes, the compact IRBF produces very accurate solutions to many fluid flow problems in comparison with some other methods such as the standard central finite different method (FDM) and HOC. Recently, Tien et al. [25] proposed a combined compact IRBF approximation scheme, where nodal first- and second-derivative values are also included in the stencil approximation, but the starting points are fourth-order derivatives. The fourth-order IRBF approach allows a more straightforward incorporation of nodal values of first- and second-order derivatives, and yields better accuracy over previous IRBF approximation schemes.

In this paper, we will incorporate the high-order combined compact IRBF approximation introduced in [25] into the fully coupled N-S approach reported in [24]. The new high-order fluid solver is verified through various problems such as heat, Burgers, convection-diffusion equations, Taylor-Green vortex and lid driven cavity flows. It will show that highly accurate results are obtained with the present approach. Then, we embed the fluid solver in the IBM procedure outlined in [26, 27] to simulate FSI problems in which a stretched elastic fibre/membrane relaxes in a viscous fluid. Comparisons between the present scheme and some others, where appropriate, are presented; and, numerical studies of the grid convergence and order of accuracy are also included.

The remainder of this paper is organised as follows: Sections 2 first reviews the spatial disretisation using the combined compact IRBF. Following this, Section 3 briefly describes the fully coupled approach for N-S equations. Section 4 summarises the mathematical formulation of the IBM. In Section 5, various numerical examples are presented and the present results are compared with some benchmark solutions, where appropriate. Finally, concluding remarks are given in Section 6.

2. Review of combined compact IRBF scheme

Consider a two-dimensional domain Ω, which is represented by a uniform Cartesian grid. The nodes are indexed in the x-direction by the subscript i ($i \in \{1, 2, ..., n_x\}$) and in the y-direction by j ($j \in \{1, 2, ..., n_y\}$). For rectangular domains, let N be the total number of nodes ($N = n_x \times n_y$) and N_{ip} be the number of interior nodes ($N_{ip} = (n_x - 2) \times (n_y - 2)$). At an interior grid point $\mathbf{x}_{i,j} = (x_{(i,j)}, y_{(i,j)})^T$ where $i \in \{2, 3, ..., n_x - 1\}$ and $j \in \{2, 3, ..., n_y - 1\}$, the associated stencils to be considered here are two local stencils: $\{x_{(i-1,j)}, x_{(i,j)}, x_{(i+1,j)}\}$ in the x-direction and $\{y_{(i,j-1)}, y_{(i,j)}, y_{(i,j+1)}\}$ in the y-direction. Hereafter, for brevity, η denotes either x or y in a generic local stencil $\{\eta_1, \eta_2, \eta_3\}$, where $\eta_1 < \eta_2 < \eta_3$, as illustrated in Figure 1.

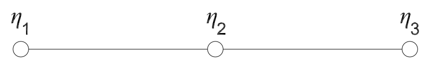

Figure 1: Compact 3-point 1D-IRBF stencil for interior nodes.

The integral process of the present combined compact IRBF starts with the decomposition of fourth-order derivatives of a variable, u, into RBFs

$$\frac{d^4u(\eta)}{d\eta^4} = \sum_{i=1}^{m} w_i G_i(\eta). \tag{1}$$

Approximate representations for the third- to first-order derivatives and the functions itself are then obtained through the integration processes

$$\frac{d^3u(\eta)}{d\eta^3} = \sum_{i=1}^{m} w_i I_{1i}(\eta) + c_1, \tag{2}$$

$$\frac{d^2u(\eta)}{d\eta^2} = \sum_{i=1}^{m} w_i I_{2i}(\eta) + c_1\eta + c_2, \tag{3}$$

$$\frac{du(\eta)}{d\eta} = \sum_{i=1}^{m} w_i I_{3i}(\eta) + \frac{1}{2}c_1\eta^2 + c_2\eta + c_3, \tag{4}$$

$$u(\eta) = \sum_{i=1}^{m} w_i I_{4i}(\eta) + \frac{1}{6}c_1\eta^3 + \frac{1}{2}c_2\eta^2 + c_3\eta + c_4, \tag{5}$$

where $I_{1i}(\eta) = \int G_i(\eta)d\eta$; $I_{2i}(\eta) = \int I_{1i}(\eta)d\eta$; $I_{3i}(\eta) = \int I_{2i}(\eta)d\eta$; $I_{4i}(\eta) = \int I_{3i}(\eta)d\eta$; and, c_1, c_2, c_3, and c_4 are the constants of integration. The analytic form of the IRBFs up to eighth-order can be found in [28]. It is noted that, for the solution of second-order PDEs, only (3-5) are needed.

2.1. First-order derivative approximations

For the combined compact approximation of the first-order derivatives at interior nodes, extra information is chosen as not only $\left\{\frac{du_1}{d\eta}; \frac{du_3}{d\eta}\right\}$ but also $\left\{\frac{d^2u_1}{d\eta^2}; \frac{d^2u_3}{d\eta^2}\right\}$. We construct the conversion system over a 3-point stencil as follows.

$$\begin{bmatrix} u_1 \\ u_2 \\ u_3 \\ \frac{du_1}{d\eta} \\ \frac{du_3}{d\eta} \\ \frac{d^2u_1}{d\eta^2} \\ \frac{d^2u_3}{d\eta^2} \end{bmatrix} = \underbrace{\begin{bmatrix} \mathbf{I}_4 \\ \mathbf{I}_3 \\ \mathbf{I}_2 \end{bmatrix}}_{\mathbf{C}} \begin{bmatrix} w_1 \\ w_2 \\ w_3 \\ c_1 \\ c_2 \\ c_3 \\ c_4 \end{bmatrix}, \tag{6}$$

where $\frac{du_i}{d\eta} = \frac{du}{d\eta}(\eta_i)$ with $i \in \{1, 2, 3\}$; $\mathbf{C}$ is the conversion matrix; and, $\mathbf{I}_2$, $\mathbf{I}_3$, and $\mathbf{I}_4$ are defined as

$$\mathbf{I}_2 = \begin{bmatrix} I_{21}(\eta_1) & I_{22}(\eta_1) & I_{23}(\eta_1) & \eta_1 & 1 & 0 & 0 \\ I_{21}(\eta_3) & I_{22}(\eta_3) & I_{23}(\eta_3) & \eta_3 & 1 & 0 & 0 \end{bmatrix}. \tag{7}$$

$$\mathbf{I}_3 = \begin{bmatrix} I_{31}(\eta_1) & I_{32}(\eta_1) & I_{33}(\eta_1) & \frac{1}{2}\eta_1^2 & \eta_1 & 1 & 0 \\ I_{31}(\eta_3) & I_{32}(\eta_3) & I_{33}(\eta_3) & \frac{1}{2}\eta_3^2 & \eta_3 & 1 & 0 \end{bmatrix}. \tag{8}$$

$$\mathbf{I}_4 = \begin{bmatrix} I_{41}(\eta_1) & I_{42}(\eta_1) & I_{43}(\eta_1) & \frac{1}{6}\eta_1^3 & \frac{1}{2}\eta_1^2 & \eta_1 & 1 \\ I_{41}(\eta_2) & I_{42}(\eta_2) & I_{43}(\eta_2) & \frac{1}{6}\eta_2^3 & \frac{1}{2}\eta_2^2 & \eta_2 & 1 \\ I_{41}(\eta_3) & I_{42}(\eta_3) & I_{43}(\eta_3) & \frac{1}{6}\eta_3^3 & \frac{1}{2}\eta_3^2 & \eta_3 & 1 \end{bmatrix}. \tag{9}$$

Solving (6) yields

$$\begin{bmatrix} w_1 \\ w_2 \\ w_3 \\ c_1 \\ c_2 \\ c_3 \\ c_4 \end{bmatrix} = \mathbf{C}^{-1} \begin{bmatrix} u_1 \\ u_2 \\ u_3 \\ \frac{du_1}{d\eta} \\ \frac{du_3}{d\eta} \\ \frac{d^2u_1}{d\eta^2} \\ \frac{d^2u_3}{d\eta^2} \end{bmatrix}, \tag{10}$$

which maps the vector of nodal values of the function and its first- and second-order derivatives to the vector of RBF coefficients including the four integration constants. The first-order derivative at the middle point is computed by substituting (10) into (4) and taking $\eta = \eta_2$

$$\frac{du_2}{d\eta} = \underbrace{\mathbf{I}_{3m}\mathbf{C}^{-1}}_{\mathbf{D}_1} \begin{bmatrix} \mathbf{u} \\ \frac{du_1}{d\eta} \\ \frac{du_3}{d\eta} \\ \frac{d^2u_1}{d\eta^2} \\ \frac{d^2u_3}{d\eta^2} \end{bmatrix}, \tag{11}$$

or

$$\frac{du_2}{d\eta} = \mathbf{D}_1(1:3)\mathbf{u} + \mathbf{D}_1(4:5)\begin{bmatrix} \frac{du_1}{d\eta} \\ \frac{du_3}{d\eta} \end{bmatrix} + \mathbf{D}_1(6:7)\begin{bmatrix} \frac{d^2u_1}{d\eta^2} \\ \frac{d^2u_3}{d\eta^2} \end{bmatrix}, \tag{12}$$

where $\mathbf{D}_1$ is a row vector of length 7, the associated notation "$a:b$" is used to indicate the vector entries from the the column a to b; $\mathbf{u} = [u_1, u_2, u_3]^T$; and,

$$\mathbf{I}_{3m} = \begin{bmatrix} I_{31}(\eta_2) & I_{32}(\eta_2) & I_{33}(\eta_2) & \frac{1}{2}\eta_2^2 & \eta_2 & 1 & 0 \end{bmatrix}. \tag{13}$$

By taking derivative terms to the left side and nodal variable values to the right side, (12) reduces to

$$\begin{bmatrix} -\mathbf{D}_1(4) & 1 & -\mathbf{D}_1(5) \end{bmatrix}\mathbf{u}' + \begin{bmatrix} -\mathbf{D}_1(6) & 0 & -\mathbf{D}_1(7) \end{bmatrix}\mathbf{u}'' = \mathbf{D}_1(1:3)\mathbf{u}, \tag{14}$$

92 where $\mathbf{u}' = \left[\frac{du_1}{d\eta}, \frac{du_2}{d\eta}, \frac{du_3}{d\eta}\right]^T$ and $\mathbf{u}'' = \left[\frac{d^2u_1}{d\eta^2}, \frac{d^2u_2}{d\eta^2}, \frac{d^2u_3}{d\eta^2}\right]^T$.

At the boundary nodes, the first-order derivatives are approximated in special compact stencils. Consider the boundary node, e.g. η_1. Its associated stencil is $\{\eta_1, \eta_2, \eta_3, \eta_4\}$ as shown in Figure 2 and extra information is chosen

Figure 2: Special compact 4-point 1D-IRBF stencil for boundary nodes.

as $\frac{du_2}{d\eta}$ and $\frac{d^2u_2}{d\eta^2}$. The conversion system over this special stencil is presented as the following matrix-vector multiplication

$$\begin{bmatrix} u_1 \\ u_2 \\ u_3 \\ u_4 \\ \frac{du_2}{d\eta} \\ \frac{d^2u_2}{d\eta^2} \end{bmatrix} = \underbrace{\begin{bmatrix} \mathbf{I}_{4sp} \\ \mathbf{I}_{3sp} \\ \mathbf{I}_{2sp} \end{bmatrix}}_{\mathbf{C}_{sp}} \begin{bmatrix} w_1 \\ w_2 \\ w_3 \\ w_4 \\ c_1 \\ c_2 \\ c_3 \\ c_4 \end{bmatrix}, \tag{15}$$

where $\mathbf{C}_{sp}$ is the conversion matrix; and, $\mathbf{I}_{2sp}$, $\mathbf{I}_{3sp}$, and $\mathbf{I}_{4sp}$ are defined as

$$\mathbf{I}_{2sp} = \begin{bmatrix} I_{21}(\eta_2) & I_{22}(\eta_2) & I_{23}(\eta_2) & I_{24}(\eta_2) & \eta_2 & 1 & 0 & 0 \end{bmatrix}. \tag{16}$$

$$\mathbf{I}_{3sp} = \begin{bmatrix} I_{31}(\eta_2) & I_{32}(\eta_2) & I_{33}(\eta_2) & I_{34}(\eta_2) & \frac{1}{2}\eta_2^2 & \eta_2 & 1 & 0 \end{bmatrix}. \tag{17}$$

$$\mathbf{I}_{4sp} = \begin{bmatrix} I_{41}(\eta_1) & I_{42}(\eta_1) & I_{43}(\eta_1) & I_{44}(\eta_1) & \frac{1}{6}\eta_1^3 & \frac{1}{2}\eta_1^2 & \eta_1 & 1 \\ I_{41}(\eta_2) & I_{42}(\eta_2) & I_{43}(\eta_2) & I_{44}(\eta_2) & \frac{1}{6}\eta_2^3 & \frac{1}{2}\eta_2^2 & \eta_2 & 1 \\ I_{41}(\eta_3) & I_{42}(\eta_3) & I_{43}(\eta_3) & I_{44}(\eta_3) & \frac{1}{6}\eta_3^3 & \frac{1}{2}\eta_3^2 & \eta_3 & 1 \\ I_{41}(\eta_4) & I_{42}(\eta_4) & I_{43}(\eta_4) & I_{44}(\eta_4) & \frac{1}{6}\eta_4^3 & \frac{1}{2}\eta_4^2 & \eta_4 & 1 \end{bmatrix}. \tag{18}$$

Solving (15) yields

$$\begin{bmatrix} w_1 \\ w_2 \\ w_3 \\ w_4 \\ c_1 \\ c_2 \\ c_3 \\ c_4 \end{bmatrix} = \mathbf{C}_{sp}^{-1} \begin{bmatrix} u_1 \\ u_2 \\ u_3 \\ u_4 \\ \frac{du_2}{d\eta} \\ \frac{d^2u_2}{d\eta^2} \end{bmatrix}. \tag{19}$$

The boundary value of the first-order derivative of u is thus obtained by substituting (19) into (4) and taking $\eta = \eta_1$

$$\frac{du_1}{d\eta} = \underbrace{\mathbf{I}_{3b}\mathbf{C}_{sp}^{-1}}_{\mathbf{D}_{1sp}} \begin{bmatrix} \mathbf{u} \\ \frac{du_2}{d\eta} \\ \frac{d^2u_2}{d\eta^2} \end{bmatrix}, \tag{20}$$

or

$$\frac{du_1}{d\eta} = \mathbf{D}_{1sp}(1:4)\mathbf{u} + \mathbf{D}_{1sp}(5)\frac{du_2}{d\eta} + \mathbf{D}_{1sp}(6)\frac{d^2u_2}{d\eta^2}, \tag{21}$$

where $\mathbf{u} = [u_1, u_2, u_3, u_4]^T$ and

$$\mathbf{I}_{3b} = \begin{bmatrix} I_{31}(\eta_1) & I_{32}(\eta_1) & I_{33}(\eta_1) & I_{34}(\eta_1) & \frac{1}{2}\eta_1^2 & \eta_1 & 1 & 0 \end{bmatrix}. \tag{22}$$

By taking derivative terms to the left side and nodal variable values to the right side, (21) reduces to

$$\begin{bmatrix} 1 & -\mathbf{D}_{1sp}(5) & 0 & 0 \end{bmatrix}\mathbf{u}' + \begin{bmatrix} 0 & -\mathbf{D}_{1sp}(6) & 0 & 0 \end{bmatrix}\mathbf{u}'' = \mathbf{D}_{1sp}(1:4)\mathbf{u}, \tag{23}$$

where $\mathbf{u}' = \left[\frac{du_1}{d\eta}, \frac{du_2}{d\eta}, \frac{du_3}{d\eta}, \frac{du_4}{d\eta}\right]^T$ and $\mathbf{u}'' = \left[\frac{d^2u_1}{d\eta^2}, \frac{d^2u_2}{d\eta^2}, \frac{d^2u_3}{d\eta^2}, \frac{d^2u_4}{d\eta^2}\right]^T$.

2.2. Second-order derivative approximations

For the combined compact approximation of the second-order derivatives at interior nodes, we employ the same extra information used in the approximation of the first-order derivative, involving $\left\{\frac{du_1}{d\eta}; \frac{du_3}{d\eta}\right\}$ and $\left\{\frac{d^2u_1}{d\eta^2}; \frac{d^2u_3}{d\eta^2}\right\}$. Therefore, the second-order derivative at the middle point is computed by simply substituting (10) into (3) and taking $\eta = \eta_2$

$$\frac{d^2u_2}{d\eta^2} = \underbrace{\mathbf{I}_{2m}\mathbf{C}^{-1}}_{\mathbf{D}_2} \begin{bmatrix} \mathbf{u} \\ \frac{du_1}{d\eta} \\ \frac{du_3}{d\eta} \\ \frac{d^2u_1}{d\eta^2} \\ \frac{d^2u_3}{d\eta^2} \end{bmatrix}, \tag{24}$$

or

$$\frac{d^2u_2}{d\eta^2} = \mathbf{D}_2(1:3)\mathbf{u} + \mathbf{D}_2(4:5) \begin{bmatrix} \frac{du_1}{d\eta} \\ \frac{du_3}{d\eta} \end{bmatrix} + \mathbf{D}_2(6:7) \begin{bmatrix} \frac{d^2u_1}{d\eta^2} \\ \frac{d^2u_3}{d\eta^2} \end{bmatrix}, \tag{25}$$

where $\mathbf{u} = [u_1, u_2, u_3]^T$ and

$$\mathbf{I}_{2m} = \begin{bmatrix} I_{21}(\eta_2) & I_{22}(\eta_2) & I_{23}(\eta_2) & \eta_2 & 1 & 0 & 0 \end{bmatrix}. \tag{26}$$

By taking derivative terms to the left side and nodal variable values to the right side, (25) reduces to

$$\begin{bmatrix} -\mathbf{D}_2(4) & 0 & -\mathbf{D}_2(5) \end{bmatrix} \mathbf{u}' + \begin{bmatrix} -\mathbf{D}_2(6) & 1 & -\mathbf{D}_2(7) \end{bmatrix} \mathbf{u}'' = \mathbf{D}_2(1:3)\mathbf{u}, \tag{27}$$

where $\mathbf{u}' = \left[\frac{du_1}{d\eta}, \frac{du_2}{d\eta}, \frac{du_3}{d\eta}\right]^T$ and $\mathbf{u}'' = \left[\frac{d^2u_1}{d\eta^2}, \frac{d^2u_2}{d\eta^2}, \frac{d^2u_3}{d\eta^2}\right]^T$.

At the boundary nodes, i.e. $\eta = \eta_1$, we employ the same special stencil, i.e. $\{\eta_1, \eta_2, \eta_3, \eta_4\}$, and extra information, i.e. $\frac{du_2}{d\eta}$ and $\frac{d^2u_2}{d\eta^2}$, used in the approximation of the first-order derivatives. Therefore, approximate expression for the second-order derivative at η_1 in the physical space is obtained by simply substituting (19) into (3) and taking $\eta = \eta_1$

$$\frac{d^2 u_1}{d\eta^2} = \underbrace{\mathbf{I}_{2b}\mathbf{C}_{sp}^{-1}}_{\mathbf{D}_{2sp}} \begin{bmatrix} \mathbf{u} \\ \frac{du_2}{d\eta} \\ \frac{d^2 u_2}{d\eta^2} \end{bmatrix}, \tag{28}$$

or

$$\frac{d^2 u_1}{d\eta^2} = \mathbf{D}_{2sp}(1:4)\mathbf{u} + \mathbf{D}_{2sp}(5)\frac{du_2}{d\eta} + \mathbf{D}_{2sp}(6)\frac{d^2 u_2}{d\eta^2}, \tag{29}$$

where $\mathbf{u} = [u_1, u_2, u_3, u_4]^T$ and

$$\mathbf{I}_{2b} = \begin{bmatrix} I_{21}(\eta_1) & I_{22}(\eta_1) & I_{23}(\eta_1) & I_{24}(\eta_1) & \eta_1 & 1 & 0 & 0 \end{bmatrix}. \tag{30}$$

By taking derivative terms to the left side and nodal variable values to the right side, (29) reduces to

$$\begin{bmatrix} 0 & -\mathbf{D}_{2sp}(5) & 0 & 0 \end{bmatrix}\mathbf{u}' + \begin{bmatrix} 1 & -\mathbf{D}_{2sp}(6) & 0 & 0 \end{bmatrix}\mathbf{u}'' = \mathbf{D}_{2sp}(1:4)\mathbf{u}, \tag{31}$$

where $\mathbf{u}' = \left[\frac{du_1}{d\eta}, \frac{du_2}{d\eta}, \frac{du_3}{d\eta}, \frac{du_4}{d\eta}\right]^T$ and $\mathbf{u}'' = \left[\frac{d^2u_1}{d\eta^2}, \frac{d^2u_2}{d\eta^2}, \frac{d^2u_3}{d\eta^2}, \frac{d^2u_4}{d\eta^2}\right]^T$.

2.3. Matrix assembly for first- and second-order derivative approximations

The IRBF system on a grid line for the first-order derivative is obtained by letting the interior node take values from 2 to $(n_\eta - 1)$ in (14); and, making use of (23) for the boundary nodes 1 and n_η. In a similar manner, the IRBF system on a grid line for the second-order derivative is obtained by letting the interior node take values from 2 to $(n_\eta - 1)$ in (27); and, making use of (31) for the boundary nodes 1 and n_η. The resultant matrix assembly is expressed as

$$\underbrace{\begin{bmatrix} \mathbf{A}_1 & \mathbf{B}_1 \\ \mathbf{A}_2 & \mathbf{B}_2 \end{bmatrix}}_{\text{Coefficient matrix}} \begin{bmatrix} \mathbf{u}'^n \\ \mathbf{u}''^n \end{bmatrix} = \begin{bmatrix} \mathbf{R}_1 \\ \mathbf{R}_2 \end{bmatrix} \mathbf{u}^n \ , \tag{32}$$

where $\mathbf{A}_1$, $\mathbf{A}_2$, $\mathbf{B}_1$, $\mathbf{B}_2$, $\mathbf{R}_1$, and $\mathbf{R}_2$ are $n_\eta \times n_\eta$ matrices; $\mathbf{u}'^n = \left[{u'_1}^n, {u'_2}^n, ..., {u'_{n_\eta}}^n \right]^T$; $\mathbf{u}''^n = \left[{u''_1}^n, {u''_2}^n, ..., {u''_{n_\eta}}^n \right]^T$; and, $\mathbf{u}^n = \left[{u_1}^n, {u_2}^n, ..., {u_{n_\eta}}^n \right]^T$. The coefficient matrix is sparse with diagonal sub-matrices. Solving (32) yields

$$\mathbf{u}'^n = \mathbf{D}_\eta \mathbf{u}^n, \tag{33}$$

$$\mathbf{u}''^n = \mathbf{D}_{\eta\eta} \mathbf{u}^n, \tag{34}$$

where $\mathbf{D}_\eta$ and $\mathbf{D}_{\eta\eta}$ are $n_\eta \times n_\eta$ matrices.

2.4. Numerical implementation

For convenience in terms of numerical implementation, the formulation developed in Section 2.1 to 2.3 can be written in an intrinsic coordinate system as shown in Figure 3 (top).

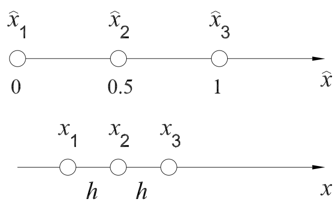

Figure 3: Intrinsic coordinate system (top), $\hat{x}$, and actual coordinate system (bottom), x, in which h is actual grid size.

The relationship between the derivatives in the intrinsic coordinate system and the corresponding ones in the actual coordinate system with a particular grid size, h, Figure 3 (bottom), is as follows.

$$\frac{du}{dx} = \frac{du}{d\hat{x}}\frac{d\hat{x}}{dx} = \frac{1}{2h}\frac{du}{d\hat{x}}. \tag{35}$$

$$\frac{d^2u}{dx^2} = \frac{1}{(2h)^2}\frac{d^2u}{d\hat{x}^2}. \tag{36}$$

Thus, the conversion matrix, $\mathbf{C}$, needs be computed and inverted once. Subsequently, as the grid size h changes, these matrices can be obtained by a simple factor.

The present compact IRBF stencils can be extended to the three-dimensional case since their approximations in each direction are constructed independently. As shown above, the IRBF approximation expressions are first derived in 1D and they are utilised to form the approximations in 2D. This procedure is also applicable to the 3D case.

3. Review of fully coupled procedure for Navier-Stokes

The transient N-S equations for an incompressible viscous fluid in the primitive variables are expressed in the dimensionless non-conservative forms as follows.

$$\frac{\partial u}{\partial t} + \underbrace{\left\{u\frac{\partial u}{\partial x} + v\frac{\partial u}{\partial y}\right\}}_{N(u)} = -\frac{\partial p}{\partial x} + \frac{1}{Re}\underbrace{\left\{\frac{\partial^2 u}{\partial x^2} + \frac{\partial^2 u}{\partial y^2}\right\}}_{L(u)}, \tag{37}$$

$$\frac{\partial v}{\partial t} + \underbrace{\left\{u\frac{\partial v}{\partial x} + v\frac{\partial v}{\partial y}\right\}}_{N(v)} = -\frac{\partial p}{\partial y} + \frac{1}{Re}\underbrace{\left\{\frac{\partial^2 v}{\partial x^2} + \frac{\partial^2 v}{\partial y^2}\right\}}_{L(v)}, \tag{38}$$

$$\frac{\partial u}{\partial x} + \frac{\partial v}{\partial y} = 0, \tag{39}$$

where u, v and p are the velocity components in the x-, y-directions and static pressure, respectively; $Re = Ul/\nu$ is the Reynolds number, in which ν, l and U are the kinematic viscosity, characteristic length and characteristic speed of the flow, respectively. For simplicity, we employ notations $N(u)$ and $N(v)$ to represent the convective terms in the x- and y-directions, respectively; and, $L(u)$ and $L(v)$ to denote the diffusive terms in the x- and y-directions, respectively.

The temporal discretisations of (37)-(39), using the Adams-Bashforth scheme for the convective terms and Crank-Nicolson scheme for the diffusive terms, result in

$$\frac{u^n - u^{n-1}}{\Delta t} + \left\{\frac{3}{2}N(u^{n-1}) - \frac{1}{2}N(u^{n-2})\right\} = -G_x(p^{n-\frac{1}{2}}) + \frac{1}{2Re}\left\{L(u^n) + L(u^{n-1})\right\}, \tag{40}$$

$$\frac{v^n - v^{n-1}}{\Delta t} + \left\{\frac{3}{2}N(v^{n-1}) - \frac{1}{2}N(v^{n-2})\right\} = -G_y(p^{n-\frac{1}{2}}) + \frac{1}{2Re}\left\{L(v^n) + L(v^{n-1})\right\}, \tag{41}$$

$$D_x(u^n) + D_y(v^n) = 0, \tag{42}$$

where n denotes the current time level; G_x and G_y are gradients in the x- and y-directions, respectively; and, D_x and D_y are gradients in the x- and y-directions, respectively.

Taking the unknown quantities in (40)-(42) to the left hand side and the known quantities to the right hand side, and then collocating them at the interior nodal points result in the matrix-vector form

$$\begin{bmatrix} \mathbf{K} & \mathbf{0} & \mathbf{G}_x \\ \mathbf{0} & \mathbf{K} & \mathbf{G}_y \\ \mathbf{D}_x & \mathbf{D}_y & \mathbf{0} \end{bmatrix} \begin{bmatrix} \mathbf{u}^n \\ \mathbf{v}^n \\ \mathbf{p}^{n-\frac{1}{2}} \end{bmatrix} = \begin{bmatrix} \mathbf{r}_x^n \\ \mathbf{r}_y^n \\ \mathbf{0} \end{bmatrix}, \tag{43}$$

where

$$\mathbf{K} = \frac{1}{\Delta t}\left\{\mathbf{I} - \frac{\Delta t}{2Re}\mathbf{L}\right\}, \tag{44}$$

$$\mathbf{r}_x^n = \frac{1}{\Delta t}\left\{\mathbf{I} + \frac{\Delta t}{2Re}\mathbf{L}\right\}\mathbf{u}^{n-1} - \left\{\frac{3}{2}\mathbf{N}(\mathbf{u}^{n-1}) - \frac{1}{2}\mathbf{N}(\mathbf{u}^{n-2})\right\}, \tag{45}$$

$$\mathbf{r}_y^n = \frac{1}{\Delta t}\left\{\mathbf{I} + \frac{\Delta t}{2Re}\mathbf{L}\right\}\mathbf{v}^{n-1} - \left\{\frac{3}{2}\mathbf{N}(\mathbf{v}^{n-1}) - \frac{1}{2}\mathbf{N}(\mathbf{v}^{n-2})\right\}, \tag{46}$$

$\mathbf{u}^n$ and $\mathbf{v}^n$ are vectors containing the nodal values of u^n and v^n at the boundary and interior nodes, respectively, while $\mathbf{p}^{n-\frac{1}{2}}$ is a vector containing the values of $p^{n-\frac{1}{2}}$ at the interior nodes only; $\mathbf{I}$ is the identity matrix; and, $\mathbf{N}$ and $\mathbf{L}$ are the matrix operators for the approximation of the convective and diffusive terms, respectively.

4. Summary of immersed boundary method

In this section, we provide a brief overview of the IBM and the reader is referred to [26, 27] for further details. For simplicity, we consider a model problem of a two-dimensional Newtonian, incompressible fluid and a one-dimensional, closed, elastic membrane. The fluid is defined on a periodic box $\Omega = [0, 1]^2$ using the Eulerian coordinates $\mathbf{x} = (x, y)$. The fluid contains an immersed neutrally-buoyant membrane $\Gamma \subset \Omega$, using the Lagrangian coordinates $s \in [0, 1]$. It is noted that the lattice points are fixed but the boundary points are moving, and those two sets of points usually do not coincide with each other. We discretise Ω using a uniform $n_x \times n_y$ grid. Then, we set the mesh size of the immersed boundary to be $n_b = 3 \times n_x$, so that there are approximately 3 immersed boundary points per mesh width.

The IBM is mathematically defined by a set of differential equations involving a mixture of Eulerian and Lagrangian variables. The motion of the fluid-membrane is governed by the incompressible N-S equations

$$\rho\left(\frac{\partial \mathbf{u}}{\partial t}+\mathbf{u}\cdot\nabla\mathbf{u}\right)=-\nabla p+\mu\nabla^2\mathbf{u}+\mathbf{f}, \tag{47}$$

$$\nabla\cdot\mathbf{u}=0, \tag{48}$$

where $\mathbf{u}=\mathbf{u}(\mathbf{x},t)=(u(\mathbf{x},t),v(\mathbf{x},t))$ and $p=p(\mathbf{x},t)$ are the fluid velocity and pressure at location $\mathbf{x}$ and time t, respectively; ρ and μ are the constant fluid density and dynamic viscosity, respectively; and, $\mathbf{f}=\mathbf{f}(\mathbf{x},t)=(f_x(\mathbf{x},t),f_y(\mathbf{x},t))$ is the external body force through which the immersed boundary is coupled to the fluid

$$\mathbf{f}(\mathbf{x},t)=\int_\Gamma \mathbf{F}(s,t)\delta(\mathbf{x}-\mathbf{X}(s,t))ds, \tag{49}$$

where $\mathbf{X}(s,t)=(X(s,t),Y(s,t))$ is a parametric curve representing the immersed boundary configuration; the delta function $\delta(\mathbf{x})=d_h(x)d_h(y)$ is a Cartesian product of one-dimensional Dirac delta functions, which is used to spread the Lagrangian immersed boundary force from Γ onto adjacent Eulerian fluid nodes. The one-dimensional Dirac delta function is chosen as

$$d_h(r)=\begin{cases}\frac{1}{8h}\left(3-2|r|/h+\sqrt{1+4|r|/h-4\left(|r|/h\right)^2}\right), & |r|\le h,\\ \frac{1}{8h}\left(5-2|r|/h-\sqrt{-7+12|r|/h-4\left(|r|/h\right)^2}\right), & h\le |r|\le 2h,\\ 0, & \text{otherwise},\end{cases} \tag{50}$$

in which h is the grid size; and, $\mathbf{F}(s,t)$ is the elastic force density which is a function of the current immersed boundary configuration

$$\mathbf{F}(s,t)=\boldsymbol{\mathcal{F}}\left(\mathbf{X}(s,t)\right)=\sigma\frac{\partial}{\partial s}\left(\frac{\partial \mathbf{X}(s,t)}{\partial s}\left(1-\frac{\varepsilon}{|\frac{\partial \mathbf{X}(s,t)}{\partial s}|}\right)\right), \tag{51}$$

which corresponds to membrane points linked together by linear springs with spring constant σ. If we assume the equilibrium strain $\varepsilon = 0$, then (51) reduces to

$$\mathbf{F}(s,t) = \boldsymbol{\mathcal{F}}\left(\mathbf{X}(s,t)\right) = \sigma \frac{\partial^2 \mathbf{X}(s,t)}{\partial s^2}. \tag{52}$$

The final equation needed to close the system is an evolution equation for the immersed boundary, which comes from the simple requirement that Γ must travel at the local fluid velocity (the non-slip condition)

$$\frac{\partial \mathbf{X}(s,t)}{\partial t} = \mathbf{U}(\mathbf{X}(s,t),t) = \int_{\Omega} \mathbf{u}(\mathbf{x},t)\delta(\mathbf{x}-\mathbf{X}(s,t))d\mathbf{x}, \tag{53}$$

where $\mathbf{U}$ is the boundary speed. The delta function δ here imposes the Eulerian flow velocity on the adjacent Lagrangian boundary nodes.

IBM algorithm. Next, we describe the algorithm used in this work, which is a discrete version of Equations (47), (48), (49), (51), and (53). Assuming that the velocity field and the membrane position are already known at time t^{n-2}, $t^{n-3/2}$, and t^{n-1}. The procedure for updating these values to time t^n is as follows.

At half time step:

Step 1. Update position of membrane

$$\frac{\mathbf{X}^{n-1/2}(s) - \mathbf{X}^{n-1}(s)}{\Delta t/2} = \sum_{\Omega} \mathbf{u}^{n-1}\delta(\mathbf{x}-\mathbf{X}^{n-1}(s))h^2. \tag{54}$$

Step 2. Compute membrane force density

$$\mathbf{F}^{n-1/2}(s) = \boldsymbol{\mathcal{F}}\left(\mathbf{X}^{n-1/2}(s)\right). \tag{55}$$

Step 3. Calculate force coming from membrane

$$\mathbf{f}^{n-1/2}(\mathbf{x}) = \sum_{\Gamma} \mathbf{F}^{n-1/2}(s)\delta(\mathbf{x}-\mathbf{X}^{n-1/2}(s))\Delta s. \tag{56}$$

Step 4. Solve for fluid motion

$$\rho\left[\frac{\mathbf{u}^{n-1/2}-\mathbf{u}^{n-1}}{\Delta t/2}+\left\{\frac{3}{2}\mathbf{N}\left(\mathbf{u}^{n-1}\right)-\frac{1}{2}\mathbf{N}\left(\mathbf{u}^{n-2}\right)\right\}\right]$$
$$=\mathbf{G}\tilde{p}^{n-1/2}+\frac{\mu}{2}\left\{\mathbf{L}\left(\mathbf{u}^{n-1/2}\right)+\mathbf{L}\left(\mathbf{u}^{n-1}\right)\right\}+\mathbf{f}^{n-1/2}. \quad (57)$$

$$\mathbf{D}\cdot\mathbf{u}^{n-1/2}=0. \quad (58)$$

Once $\mathbf{u}^{n-1/2}$ are known, we use them to take a full step from time t^{n-1} to t^n, as follows.

At full time step:

Step 5. Solve for fluid motion

$$\rho\left[\frac{\mathbf{u}^{n}-\mathbf{u}^{n-1}}{\Delta t}+\left\{\frac{3}{2}\mathbf{N}\left(\mathbf{u}^{n-1/2}\right)-\frac{1}{2}\mathbf{N}\left(\mathbf{u}^{n-3/2}\right)\right\}\right]$$
$$=\mathbf{G}p^{n-1/2}+\frac{\mu}{2}\left\{\mathbf{L}\left(\mathbf{u}^{n}\right)+\mathbf{L}\left(\mathbf{u}^{n-1}\right)\right\}+\mathbf{f}^{n-1/2}. \quad (59)$$

$$\mathbf{D}\cdot\mathbf{u}^{n}=0. \quad (60)$$

Step 6. Update position of membrane

$$\frac{\mathbf{X}^n(s)-\mathbf{X}^{n-1}(s)}{\Delta t}=\sum_{\Omega}\mathbf{u}^{n-1/2}\delta(\mathbf{x}-\mathbf{X}^{n-1/2}(s))h^2. \quad (61)$$

5. Numerical examples

We chose the multiquadric (MQ) function as the basis function in the present calculations

$$G_i(x)=\sqrt{(x-c_i)^2+a_i^2}, \quad (62)$$

where c_i and a_i are the centre and the width of the i-th MQ, respectively. For each stencil, the set of nodal points is taken to be the same as the set of MQ centres. We simply choose the MQ width as $a_i = \beta h_i$, where β is a positive scalar and h_i is the distance between the i-th node and its closest neighbour. The value of $\beta = 10$ is chosen for calculations in the present work. We evaluate the performance of the present scheme through the following measures

i. The root mean square error (RMS) is defined as

$$RMS = \sqrt{\frac{\sum_{i=1}^{N} \left(f_i - \overline{f}_i\right)^2}{N}}, \tag{63}$$

where f_i and $\overline{f}_i$ are the computed and exact values of the solution f at the i-th node, respectively; and, N is the number of nodes over the whole domain.

ii. The maximum absolute error (L_∞) is defined as

$$L_\infty = \max_{i=1,\ldots,N} |f_i - \overline{f}_i|. \tag{64}$$

iii. The global convergence rate, α, with respect to the grid refinement is defined through

$$RMS(h) \approx \gamma h^\alpha = O(h^\alpha), \tag{65}$$

where h is the grid size; and, γ and α are exponential model's parameters.

iv. A flow is considered as reaching its steady state when

$$\sqrt{\frac{\sum_{i=1}^{N} \left(f_i^n - f_i^{n-1}\right)^2}{N}} < 10^{-9}. \tag{66}$$

v. Difference (%) between computed and analytical values is defined to be

$$\frac{f - \overline{f}}{\overline{f}} \times 100. \tag{67}$$

For comparison purposes, we also implement the standard FDM, HOC scheme of Tian et al. [15] and coupled compact IRBF scheme of Tien et al. [23] for numerical calculations.

5.1. Heat equation

By selecting the following heat equation, the performance of the present combined compact IRBF scheme can be studied for the diffusive term only as

$$\frac{\partial u}{\partial t} = \frac{\partial^2 u}{\partial x^2}, \quad a \leq x \leq b, \quad t \geq 0, \tag{68}$$

$$u(x,0) = u_0(x), \quad a \leq x \leq b, \tag{69}$$

$$u(a,t) = u_{\Gamma_1}(t) \;\text{ and }\; u(b,t) = u_{\Gamma_2}(t), \quad t \geq 0, \tag{70}$$

where u and t are the field variable and time, respectively; and, $u_0(x)$, $u_{\Gamma_1}(t)$, and $u_{\Gamma_2}(t)$ are prescribed functions. The temporal discretisation of (68) with the Crank-Nicolson scheme gives

$$\frac{u^n - u^{n-1}}{\Delta t} = \frac{1}{2}\left\{\frac{\partial^2 u^n}{\partial x^2} + \frac{\partial^2 u^{n-1}}{\partial x^2}\right\}, \tag{71}$$

where the superscript n denotes the current time step. (71) can be rewritten as

$$\left\{1 - \frac{\Delta t}{2}\frac{\partial^2}{\partial x^2}\right\} u^n = \left\{1 + \frac{\Delta t}{2}\frac{\partial^2}{\partial x^2}\right\} u^{n-1}. \tag{72}$$

Consider (68) on a segment $[0,\pi]$ with the initial and boundary conditions

$$u(x,0) = \sin(2x), \quad 0 < x < \pi. \tag{73}$$

$$u(0,t) = u(\pi,t) = 0, \quad t \geq 0. \tag{74}$$

The exact solution of this problem can be verified to be

$$\overline{u}(x,t) = \sin(2x)e^{-4t}. \tag{75}$$

The spatial accuracy of the present scheme is investigated using various uniform grids $\{11, 13, ..., 25\}$. We employ here a small time step, $\Delta t = 10^{-6}$, to minimise the effect of the approximation error in time. The solution is computed at $t = 0.0125$. Figure 4 shows that the present combined compact IRBF outperforms the standard central FDM, HOC, coupled compact IRBF in terms of both the solution accuracy and convergence rate.

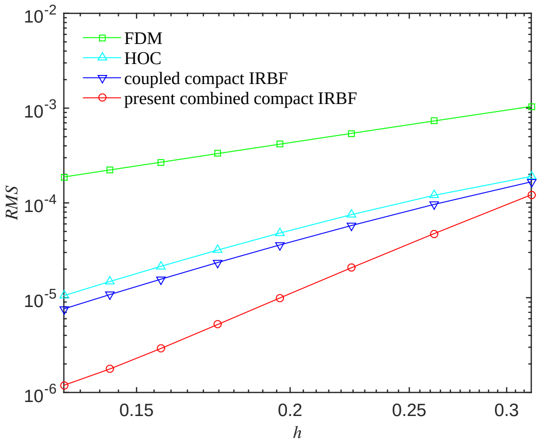

Figure 4: Heat equation, $\{11, 13, ..., 25\}$, $\Delta t = 10^{-6}$, $t = 0.0125$: The effect of the grid size h on the solution accuracy RMS. The solution converges as $O(h^{1.96})$ for the central FDM, $O(h^{3.34})$ for the HOC, $O(h^{3.54})$ for the coupled compact IRBF, and $O(h^{5.35})$ for the present combined compact IRBF.

5.2. Burgers equation

With Burgers equation, the performance of the present combined compact IRBF scheme can be investigated for both the convective and diffusive terms as

$$\frac{\partial u}{\partial t} + u\frac{\partial u}{\partial x} = \frac{1}{Re}\frac{\partial^2 u}{\partial x^2}, \quad a \le x \le b, \quad t \ge 0, \tag{76}$$

$$u(x,0) = u_0(x), \quad a \le x \le b, \tag{77}$$

$$u(a,t) = u_{\Gamma_1}(t) \text{ and } u(b,t) = u_{\Gamma_2}(t), \quad t \ge 0, \tag{78}$$

where $Re > 0$ is the Reynolds number; and, $u_0(x)$, $u_{\Gamma_1}(t)$, and $u_{\Gamma_2}(t)$ are prescribed functions. The temporal discretisations of (76) using the Adams-Bashforth scheme for the convective term and Crank-Nicolson scheme for the diffusive term, result in

$$\frac{u^n - u^{n-1}}{\Delta t} + \left\{ \frac{3}{2}\left(u\frac{\partial u}{\partial x}\right)^{n-1} - \frac{1}{2}\left(u\frac{\partial u}{\partial x}\right)^{n-2} \right\} = \frac{1}{2Re}\left\{ \frac{\partial^2 u^n}{\partial x^2} + \frac{\partial^2 u^{n-1}}{\partial x^2} \right\}, \tag{79}$$

or

$$\left\{1 - \frac{\Delta t}{2Re}\frac{\partial^2}{\partial x^2}\right\} u^n = \left\{1 + \frac{\Delta t}{2Re}\frac{\partial^2}{\partial x^2}\right\} u^{n-1} - \Delta t \left\{ \frac{3}{2}\left(u\frac{\partial u}{\partial x}\right)^{n-1} - \frac{1}{2}\left(u\frac{\partial u}{\partial x}\right)^{n-2} \right\}. \tag{80}$$

The problem is considered on a segment $0 \le x \le 1$ in the form [29]

$$\overline{u}(x,t) = \frac{\alpha_0 + \mu_0 + (\mu_0 - \alpha_0)\exp(\lambda)}{1 + \exp(\lambda)}, \tag{81}$$

where $\lambda = \alpha_0 Re(x - \mu_0 t - \beta_0)$, $\alpha_0 = 0.4$, $\beta_0 = 0.125$, $\mu_0 = 0.6$, and $Re = 200$. The initial and boundary conditions can be derived from the analytic solution (81). The calculations are carried out on a set of uniform grids $\{61, 71, ..., 121\}$. The time step $\Delta t = 10^{-6}$ is chosen. The errors of the solution are calculated at the time $t = 0.0125$. Figure 5 shows that the present combined compact IRBF overwhelms the standard central FDM, HOC, coupled compact IRBF schemes in terms of both the solution accuracy and convergence rate.

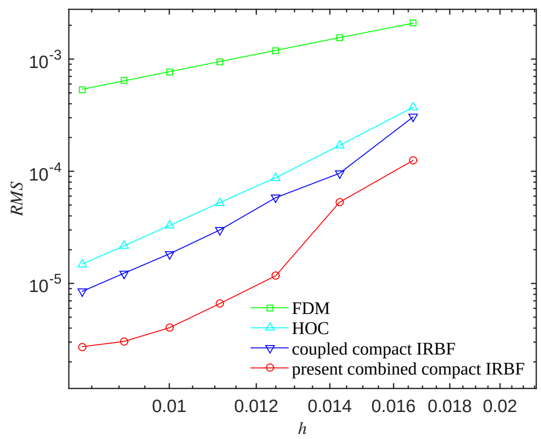

Figure 5: Burgers equation, $\{61, 71, ..., 121\}$, $Re = 200$, $\Delta t = 10^{-6}$, $t = 0.0125$: The effect of the grid size h on the solution accuracy RMS. The solution converges as $O(h^{1.96})$ for the central FDM, $O(h^{4.62})$ for the HOC, $O(h^{5.03})$ for the coupled compact IRBF, and $O(h^{5.81})$ for the present combined compact IRBF.

5.3. Convection-diffusion equations

To study the performance of the present combined compact IRBF approximation in simulating convection-diffusion problems, we employ the alternating direction implicit (ADI) procedure which was detailed in [23]. A two-dimensional unsteady convection-diffusion equation for a variable u is expressed as follows.

$$\frac{\partial u}{\partial t} + c_x \frac{\partial u}{\partial x} + c_y \frac{\partial u}{\partial y} = d_x \frac{\partial^2 u}{\partial x^2} + d_y \frac{\partial^2 u}{\partial y^2} + f_b, \quad (x, y, t) \in \Omega \times [0, T], \tag{82}$$

subject to the initial condition

$$u(x, y, 0) = u_0(x, y), \quad (x, y) \in \Omega, \tag{83}$$

and the Dirichlet boundary condition

$$u(x, y, t) = u_\Gamma(x, y, t), \quad (x, y) \in \Gamma, \tag{84}$$

where Ω is a two-dimensional rectangular domain; Γ is the boundary of Ω; $[0, T]$ is the time interval; f_b is the driving function; u_0 and u_Γ are some given functions; c_x and c_y are the convective velocities; and, d_x and d_y are the diffusive coefficients.

In this work, we consider $f_b = 0$, in a square $\Omega = [0, 2]^2$ with the following analytic solution [30]

$$\overline{u}(x, y, t) = \frac{1}{4t + 1} exp\left[-\frac{(x - c_x t - 0.5)^2}{d_x(4t + 1)} - \frac{(y - c_y t - 0.5)^2}{d_y(4t + 1)}\right], \tag{85}$$

and subject to the Dirichlet boundary condition. From (85), one can derive the initial and boundary conditions. We consider two sets of parameters

Case I: $c_x = c_y = 0.8$, $d_x = d_y = 0.01$, $t = 0.0125$, $\Delta t = 1E - 6$.

Case II: $c_x = c_y = 80$, $d_x = d_y = 0.01$, $t = 0.0125$, $\Delta t = 1E - 6$.

The corresponding Peclet number is thus $Pe = 2$ for case I and $Pe = 200$ for case II. Figures 6 and 7 show analyses of the solution accuracy when the grid size is refined. It can be seen that the accuracy and convergence rate of the present combined compact IRBF scheme are much better than those of the central FDM, HOC, and coupled compact IRBF.

5.4. Taylor-Green vortex

To study the performance of the combination of the combined compact IRBF and the fully coupled approaches in simulating viscous flow, we consider a transient flow problem, namely Taylor-Green vortex [15]. This problem is governed by the N-S equations (40)-(42) and has the analytical solutions

$$\overline{u}(x_1, x_2, t) = -\cos(kx_1)\sin(kx_2)\exp(-2k^2 t/Re), \tag{86}$$

$$\overline{v}(x_1, x_2, t) = \sin(kx_1)\cos(kx_2)\exp(-2k^2 t/Re), \tag{87}$$

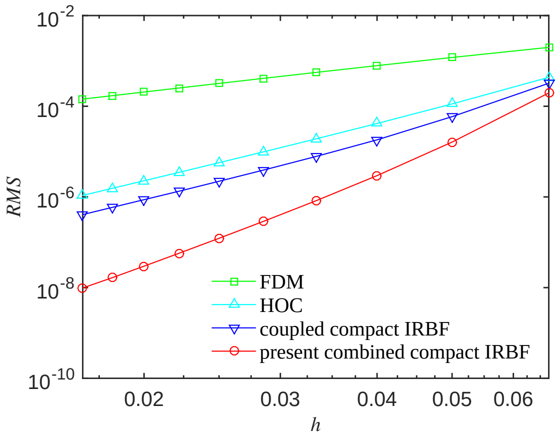

Figure 6: Unsteady convection-diffusion equation, $\{31 \times 31, 41 \times 41, ..., 121 \times 121\}$, case I: The effect of the grid size h on the solution accuracy RMS. The solution converges as $O(h^{1.90})$ for the central FDM, $O(h^{4.29})$ for the HOC, $O(h^{4.71})$ for the coupled compact IRBF, and $O(h^{7.02})$ for the present combined compact IRBF.

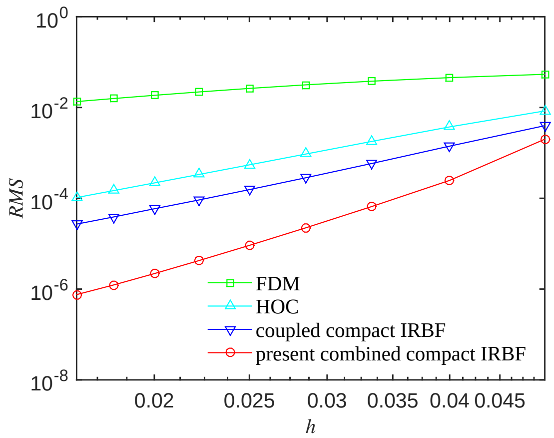

Figure 7: Unsteady convection-diffusion equation, $\{41 \times 41, 51 \times 51, ..., 121 \times 121\}$, case II: The effect of the grid size h on the solution accuracy RMS. The solution converges as $O(h^{1.28})$ for the central FDM, $O(h^{4.04})$ for the HOC, $O(h^{4.56})$ for the coupled compact IRBF, and $O(h^{7.04})$ for the present combined compact IRBF.

$$\overline{p}(x_1, x_2, t) = -1/4 \left\{\cos(2kx_1) + \cos(2kx_2)\right\} \exp(-4k^2 t/Re), \qquad (88)$$

where $0 \leq x_1, x_2 \leq 2\pi$. Calculations are carried out for $k = 2$ on a set of uniform grids, $\{11 \times 11, 21 \times 21, ..., 51 \times 51\}$. A fixed time step $\Delta t = 0.002$ and $Re = 100$ are employed. Numerical solutions are computed at $t = 2$. The exact solutions, i.e. equations (86)-(88), provide the initial field at $t = 0$ and the time-dependent boundary conditions. Table 1 shows the accuracy comparison of the present scheme with the HOC scheme of Tian et al. [15] and the compact IRBF scheme of Tien el al. [24]. It is seen that the present scheme produces much better accuracy than the two other schemes; and, its convergence rates are much higher than those of the HOC and compact IRBF, i.e. $O(h^{7.02})$ compared to $O(h^{5.35})$ of the compact IRBF and $O(h^{2.92})$ of the HOC for the u-velocity; and, $O(h^{8.51})$ compared to $O(h^{4.48})$ of the compact IRBF and $O(h^{3.28})$ of the HOC for the pressure.

5.5. Lid driven cavity

The classical lid driven cavity flow has been considered as a test problem for the evaluation of numerical methods and the validation of fluid flow solvers for the past decades. Figure 8 shows the problem definition and boundary conditions. Uniform grids of $\{31 \times 31, 51 \times 51, 71 \times 71, 91 \times 91, 111 \times 111\}$ and $Re = 1000$ are employed in the simulation. A fixed time step is chosen to be $\Delta t = 0.001$. Numerical results of the present scheme are compared with those of some others [13, 24, 31, 32, 33, 34, 35, 36]. From the literature, FDM results using very dense grids presented by Ghia et al. [31] and pseudo-spectral results presented by Botella and Peyret [13] have been referred to as "Benchmark" results for comparison purposes.

Table 1: Taylor-Green vortex: RMS-errors and convergence rates.

present combined compact IRBF			
Grid	u-error	v-error	p-error
11×11	1.0652655E+00	1.0584558E+00	6.6053162E+00
21×21	6.4466038E-04	6.3416436E-04	5.5476571E-03
31×31	1.1927530E-04	1.1745523E-04	1.6486893E-04
41×41	1.8243332E-05	1.7849839E-05	1.8919708E-05
51×51	1.4261494E-05	1.2104415E-05	1.1300027E-05
Rate	$O(h^{7.02})$	$O(h^{7.10})$	$O(h^{8.51})$
compact IRBF [24]			
Grid	u-error	v-error	p-error
11×11	1.7797233E-01	1.7797723E-01	3.0668704E-01
21×21	4.6366355E-03	4.6366340E-03	8.5913505E-03
31×31	5.3168859E-04	5.3168061E-04	2.6550518E-03
41×41	1.0970214E-04	1.0968156E-04	3.4713723E-04
51×51	3.2428099E-05	3.2378594E-05	2.6244035E-04
Rate	$O(h^{5.35})$	$O(h^{5.35})$	$O(h^{4.48})$
HOC [15]			
Grid	u-error	v-error	p-error
11×11	7.0070489E-02	7.0070489E-02	1.0764149E-01
21×21	9.0692193E-03	9.0692193E-03	1.0567607E-02
31×31	2.8851487E-03	2.8851487E-03	2.9103288E-03
41×41	1.2238736E-03	1.2238736E-03	1.1356134E-03
51×51	6.3063026E-04	6.3063026E-04	5.3933641E-04
Rate	$O(h^{2.92})$	$O(h^{2.92})$	$O(h^{3.28})$

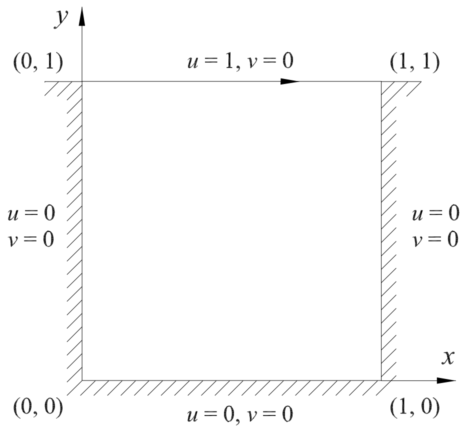

Figure 8: Lid driven cavity: problem configurations and boundary conditions.

Table 2 shows the present results for the extrema of the vertical and horizontal velocity profiles along the horizontal and vertical centrelines of the cavity. The "Errors" evaluated are relative to "Benchmark" results of [13]. With relatively coarser grids, the results obtained by the present scheme are very comparable with others using denser grids.

Figure 9 displays velocity profiles along the vertical and horizontal centrelines for different grid sizes, where the grid convergence of the present scheme is clearly observed (i.e. the present solution approaches the benchmark solution with a fast rate as the grid density is increased). The present scheme effectively achieves the benchmark results with a grid of only 71×71 in comparison with the grid of 129×129 used to obtain the benchmark results in [31]. In addition, those velocity profiles, with the grid of 71×71, are displayed in Figure 10, where the present solutions match the benchmark ones very well.

To exhibit contour plots of the flow, Figures 11 and 12 show streamlines

Table 2: Lid driven cavity, $Re = 1000$: Extrema of the vertical and horizontal velocity profiles along the horizontal and vertical centrelines of the cavity, respectively. "Errors" are relative to the "Benchmark" data.

Method	Grid	u_{min}	Error (%)	y_{min}	v_{max}	Error (%)	x_{max}	v_{min}	Error (%)	x_{min}
present combined compact IRBF	31×31	-0.3666974	5.63	0.1979	0.3550856	5.80	0.1601	-0.4851327	7.96	0.8932
present combined compact IRBF	51×51	-0.3756440	3.33	0.1760	0.3640018	3.43	0.1603	-0.5110586	3.04	0.9035
present combined compact IRBF	71×71	-0.3837160	1.25	0.1725	0.3717639	1.37	0.1590	-0.5210042	1.15	0.9078
present combined compact IRBF	91×91	-0.3866230	0.50	0.1718	0.3747332	0.59	0.1584	-0.5248188	0.43	0.9088
present combined compact IRBF	111×111	-0.3877643	0.21	0.1716	0.3759610	0.26	0.1581	-0.5262950	0.15	0.9091
compact IRBF (u, v, p), [24]	51×51	-0.3611357	7.06	0.1819	0.3481667	7.63	0.1621	-0.4853383	7.92	0.9025
compact IRBF (u, v, p), [24]	71×71	-0.3807425	2.01	0.1741	0.3685353	2.23	0.1593	-0.5156774	2.16	0.9079
compact IRBF (u, v, p), [24]	91×91	-0.3857664	0.72	0.1725	0.3738367	0.82	0.1585	-0.5231499	0.75	0.9089
compact IRBF (u, v, p), [24]	111×111	-0.3873278	0.32	0.1720	0.3755235	0.38	0.1582	-0.5254043	0.32	0.9091
compact IRBF (u, v, p), [36]	71×71	-0.3755225	3.36	0.1753	0.3637009	3.51	0.1608	-0.5086961	3.49	0.9078
compact IRBF (u, v, p), [36]	91×91	-0.3815923	1.80	0.1735	0.3698053	1.89	0.1594	-0.5174658	1.82	0.9085
compact IRBF (u, v, p), [36]	111×111	-0.3840354	1.17	0.1728	0.3722634	1.24	0.1588	-0.5209683	1.16	0.9088
compact IRBF (u, v, p), [36]	129×129	-0.3848064	0.97	0.1724	0.3729119	1.07	0.1586	-0.5223350	0.90	0.9089
FVM (u, v, p), [34]	128×128	-0.38511	0.89	—	0.37369	0.86	—	-0.5228	0.81	—
FDM ($\psi - \omega$), [31]	129×129	-0.38289	1.46	0.1719	0.37095	1.59	0.1563	-0.5155	2.20	0.9063
FEM (u, v, p), [32]	129×129	-0.375	3.49	0.160	0.362	3.96	0.160	-0.516	2.10	0.906
FDM (u, v, p), [33]	256×256	-0.3764	3.13	0.1602	0.3665	2.77	0.1523	-0.5208	1.19	0.9102
FVM (u, v, p), [35]	257×257	-0.388103	0.12	0.1727	0.376910	0.01	0.1573	-0.528447	0.26	0.9087
Benchmark, [13]		-0.3885698		0.1717	0.3769447		0.1578	-0.5270771		0.9092

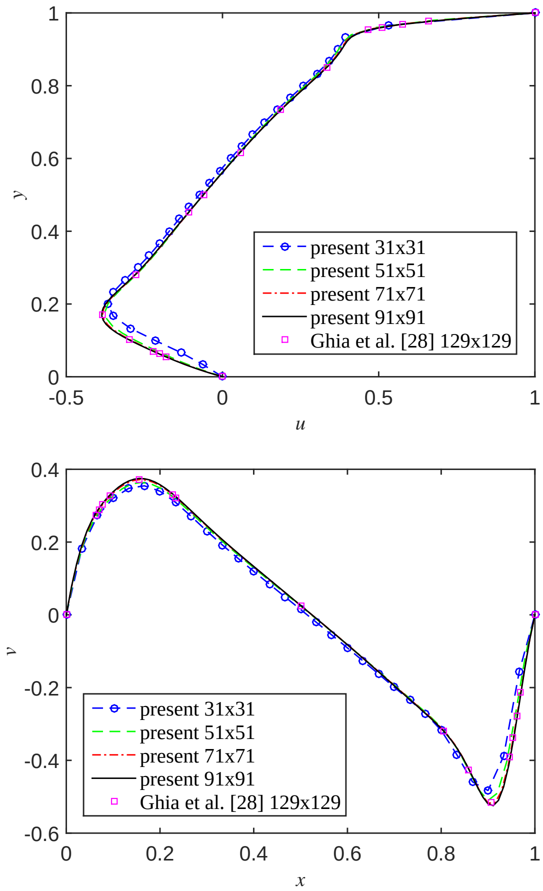

Figure 9: Lid driven cavity, $Re = 1000$: Profiles of the u-velocity along the vertical centreline (top) and the v-velocity along the horizontal centreline (bottom) as the grid density increases.

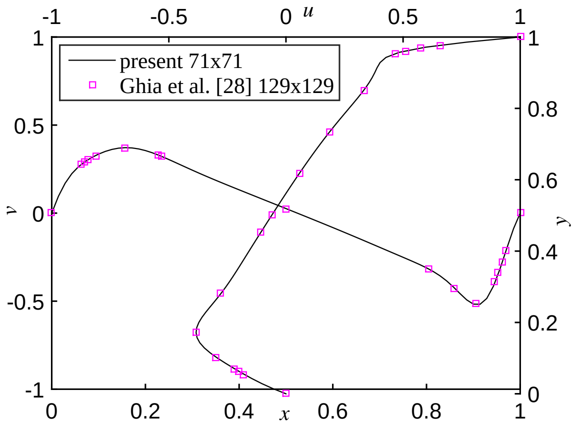

Figure 10: Lid driven cavity, $Re = 1000$: Profiles of the u-velocity along the vertical centreline and the v-velocity along the horizontal centreline.

and iso-vorticity lines, respectively, which are derived from the velocity field. Figure 13 shows the pressure deviation contours of the present simulation. These plots are also in good agreement with those reported in the literature.

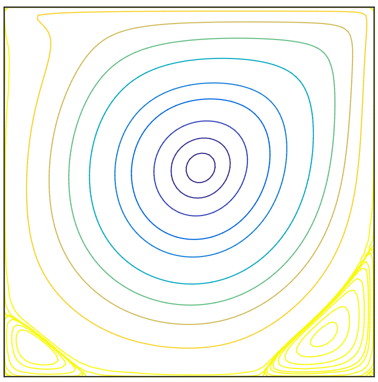

Figure 11: Lid driven cavity, $Re = 1000$, 91×91: Streamlines of the flow. The contour values used here are taken to be the same as those in [31].

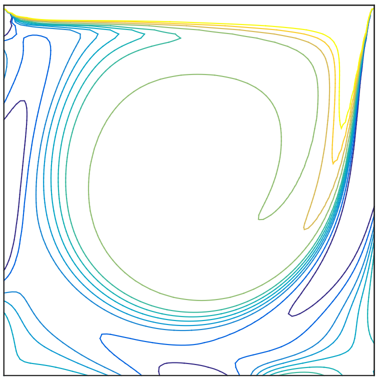

Figure 12: Lid driven cavity, Re = 1000, 91 $\times$ 91: Iso-vorticity lines of the flow. The contour values used here are taken to be the same as those in [31].

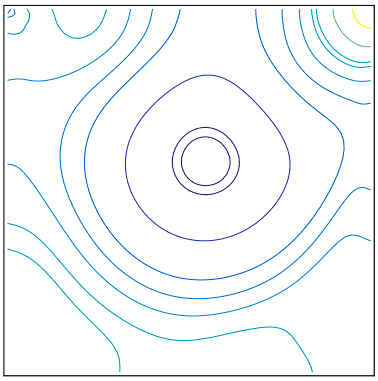

Figure 13: Lid driven cavity, Re = 1000, 91 $\times$ 91: Static pressure contours of the flow. The contour values used here are taken to be the same as those in [13].

5.6. Elastic flat fibre (surface)

To investigate the accuracy of the combined compact IRBF in solving FSI problems, we consider a flat fibre problem which was studied in [37, 38]. For comparison purposes, we set up the problem parameters and configurations to be the same as those used in [37]. Figure 14 depicts the problem configurations. The fluid domain is a unit square with periodic boundary conditions

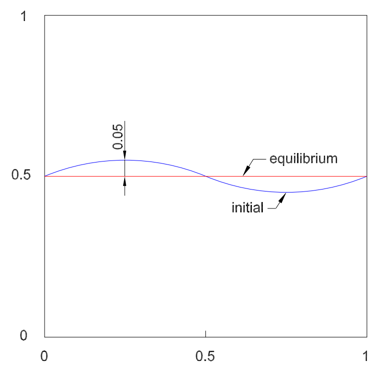

Figure 14: Fibre: The initial fibre position is a sinusoidal curve. The equilibrium state is a flat surface.

in the x- and y-directions. The viscosity and density constants are chosen as $\mu = 1$ and $\rho = 1$, respectively. The initial position is a sinusoidal curve described by

$$\mathbf{X}(s,0) = \left(s, \frac{1}{2} + A\,\sin(2\pi s)\right), \tag{89}$$

where the constant A is set to 0.05. The fluid is initially at rest

$$\mathbf{u}(\mathbf{x},0) = 0. \tag{90}$$

The purpose of this simulation is to test the decay rate of the maximum height of the fibre. Figure 15 plots a sample of the computed maximum height of the immersed fibre as a function of time, which oscillates with a decaying amplitude. There are two quantities that can easily be obtained from this information in order to make comparisons with the analytic results [37]:

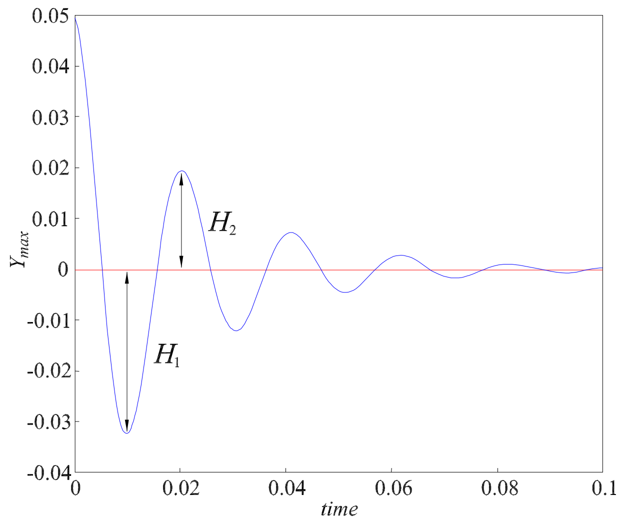

Figure 15: Fibre: A sample of computed maximum fibre height versus time.

i. The decay rate, $Dr(\lambda)$, for the smallest wave number 2π mode which can be determined by measuring the rate at which the maximum fibre height decays to zero

$$Dr(\lambda) = \frac{1}{t_2 - t_1} ln \left(\frac{H_2}{H_1} \right). \tag{91}$$

ii. The frequency, $Fr(\lambda)$, which can be calculated from the period of the fibre oscillations

$$Fr(\lambda) = \frac{\pi}{t_2 - t_1}. \tag{92}$$

The results are summarised in Table 3 for various values of the fibre spring constant $\sigma = \{1, 20, 100, 1000, 10000, 100000\}$. With relatively coarse grids, the present decay rate shows very good agreement with the analytical results, and so does the frequency. The relative difference is within 6.3% for all values of σ. The decay rates produced by the present scheme are generally more

Table 3: Fibre: Analytical and computed values of the decay rate $Dr(\lambda)$ and frequency $Fr(\lambda)$ for the solution mode with the smallest wave number 2π. The difference is computed relative to the analytical value.

present combined compact IRBF									
Parameters				Smallest decay rate $Dr(\lambda)$			Frequency $Fr(\lambda)$		
σ	$n_x \times n_y$	n_b	Δt	Computed	Analytical	Difference (%)	Computed	Analytical	Difference (%)
1	40×40	120	1×10^{-2}	-1.6	-1.6	0.0	1	0	—
20	40×40	120	1×10^{-3}	-25	-26	3.8	28	28	0.0
100	40×40	120	5×10^{-4}	-33	-33	0.0	84	86	2.3
1000	40×40	120	2×10^{-4}	-49	-51	3.9	302	310	2.6
10000	60×60	180	2×10^{-5}	-80	-84	4.8	1033	1039	0.6
100000	100×100	300	2×10^{-6}	-133	-142	6.3	3364	3390	0.8
FDM [37]									
Parameters				Smallest decay rate $Dr(\lambda)$			Frequency $Fr(\lambda)$		
σ	$n_x \times n_y$	n_b	Δt	Computed	Analytical	Difference (%)	Computed	Analytical	Difference (%)
1	64×64	192	—	-1.5	-1.6	6.3	0	0	—
20	64×64	192	—	-24	-26	7.7	30	28	7.1
100	64×64	192	—	-32	-33	3.0	85	86	1.2
1000	64×64	192	—	-46	-51	9.8	310	310	0.0
10000	64×64	192	—	-75	-84	10.7	1030	1039	0.9
100000	64×64	192	—	-131	-142	7.7	3360	3390	0.9

accurate than those of the FDM reported in [37].

To measure the effect of the spatial discretisation on the solution accuracy, we compute the problem on successively finer grids $\{20\times 20, 40\times 40, ..., 140\times 140\}$. Table 4 lists a series of computations for $\sigma = 100000$ at which the largest discrepancy between the computed and analytical decay rates occurs. The difference between the computed and analytical results decreases as the

Table 4: Fibre, $\sigma = 100000$, and $\Delta t = 2\times 10^{-6}$: Grid convergence of λ to the analytical value $\lambda \approx -142 + 3390\, i$. The maximum norm errors are based on comparisons between the computed decay rate $Dr(\lambda)$ and the analytical decay rate of -142.

present combined compact IRBF				
$n_x \times n_y$	$Dr(\lambda)$	$Fr(\lambda)$	Error	Local rate$^{(*)}$
20×20	-69	3027	73	—
40×40	-96	3279	46	0.7
60×60	-117	3342	25	1.5
80×80	-127	3349	15	1.7
100×100	-133	3364	9	2.3
120×120	-137	3378	5	3.6
140×140	-140	3378	2	4.6
FDM [37]				
$n_x \times n_y$	$Dr(\lambda)$	$Fr(\lambda)$	Error	Local rate$^{(*)}$
16×16	-73	2960	69	—
32×32	-100	3260	42	0.7
64×64	-131	3360	11	1.9
128×128	-147	3370	5	1.1
256×256	-140	3370	2	1.3

$^{(*)}$Local rate=-log$[error_{new}/error_{old}]$/log$[n_{xnew}/n_{xold}]$.

number of grid points increases; while, the local convergence rate does not settle down to any value, it does appear to be in between first- and fourth-order spatial accuracy. It can be seen that the present combined compact IRBF, with the much coarser grid of only 140×140, reaches the same level of accuracy of the FDM using the very dense grid of 256×256 as presented in [37].

Using the parameters described in Table 3, we plot the evolution of Y_{max} towards the equilibrium condition as shown in Figure 16, which shows that the computed solutions converge to the correct steady state. In Figure 17, the profiles of the fibre and the velocity and pressure fields at various times are plotted. These plots are in good agreement with those reported in [38]. In Figure 18, we plot the u- and v-velocity profiles along the horizontal and vertical centrelines, respectively, with the grid refinement for $\sigma = 100000$ at $t = 0.005$. It can be seen that the solution converges at the grid of 120×120.

5.7. Enclosed elastic tubular membrane

We now consider another FSI problem, a stretched pressurised tubular membrane immersed in a viscous fluid, which is a typical test for FSI solvers seen in the literature to date [37, 39, 40, 41, 42, 43, 44, 45, 46]. For comparison, we deliberately set parameters and conditions of the problem to be the same as those used in [37, 40, 45]. We assume that the inflated and stretched shape of the membrane is defined as an ellipse with major and minor radii $a = 0.4$ and $b = 0.2$, respectively. Due to the restoring force of the elastic boundary and the incompressibility of the fluid inside the membrane, when the membrane is relaxed its shape should converge to an equilibrium circular steady state with radius $r = \sqrt{ab} \approx 0.2828$. The initial and equilibrium

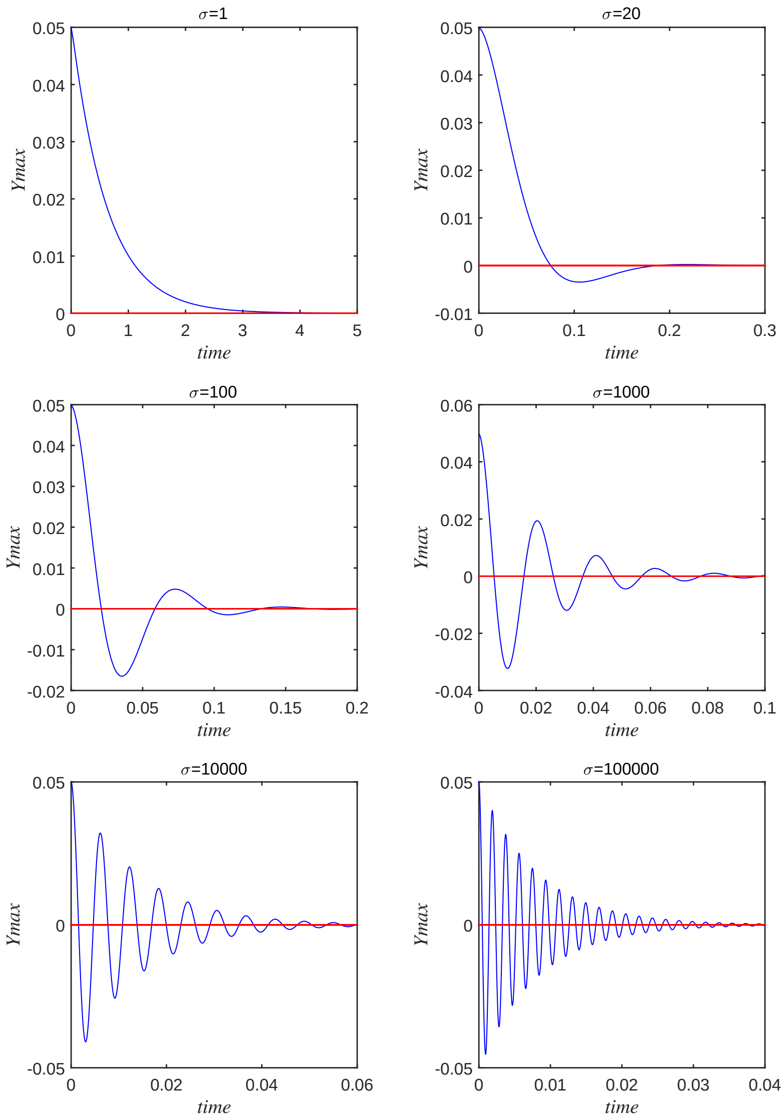

Figure 16: Fibre: Evolution of Y_{max} for different spring constants. The fibre oscillates as it converges to the equilibrium state.

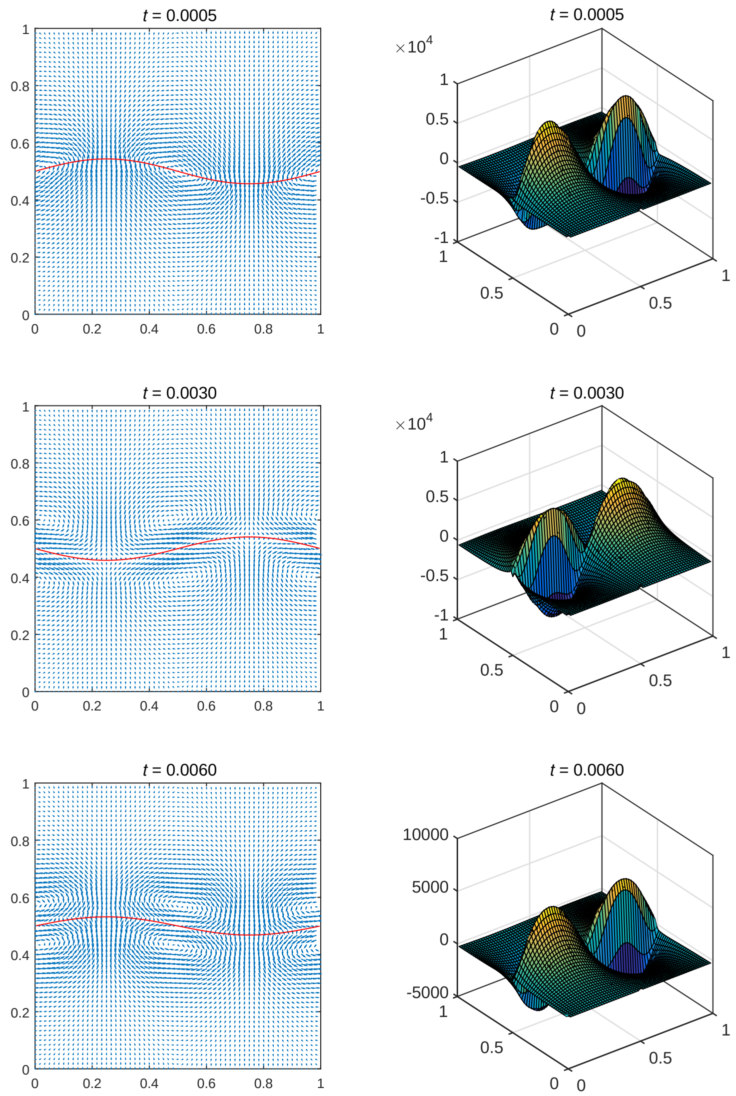

Figure 17: Fibre, $\sigma = 10000$, $n_x = n_y = 60$, $n_b = 180$, and $\Delta t = 2 \times 10^{-5}$: Velocity field and profiles of the fibre (left hand column); and, pressure field (right hand column) at three different times.

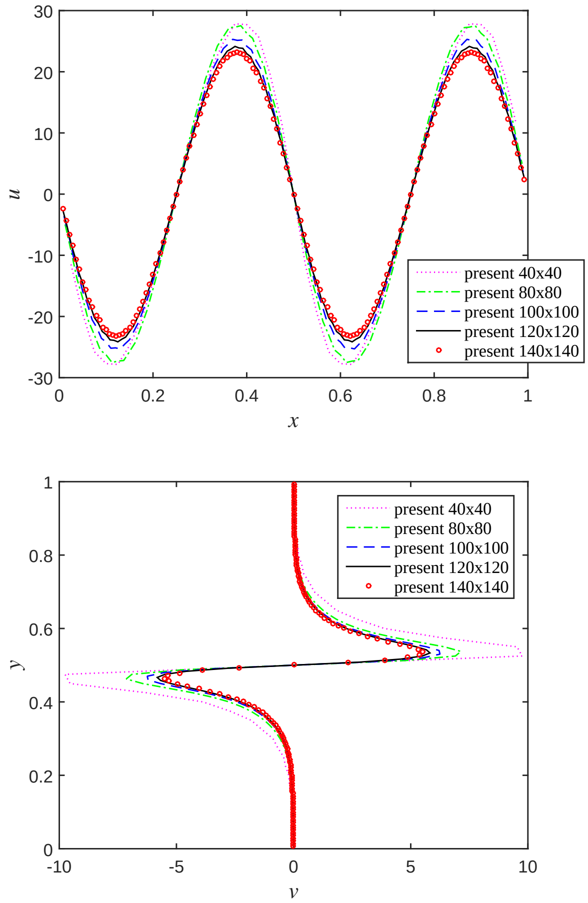

Figure 18: Fibre, $\sigma = 100000$, $\Delta t = 2\times10^{-6}$, and $t = 0.005$: Profiles of the u-velocity along the horizontal centreline (top) and the v-velocity along the vertical centreline (bottom). It is noted that the curves for the last two grids are almost indistinguishable, which shows that the solution converges at the grid of 120×120.

positions of the elastic membrane are depicted in Figure 19. We supplement

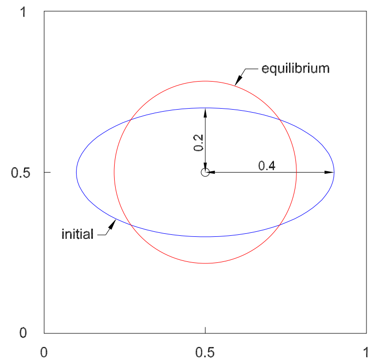

Figure 19: Tubular membrane: The initial membrane configuration is a tube with elliptical cross section with semi-axes 0.4 and 0.2. The equilibrium state is a circular tube with a radius approximately 0.2828.

the system of equations described in Section 4 with the initial conditions

$$\mathbf{X}(s,0) = \left(\frac{1}{2} + a\,\cos(2\pi s), \frac{1}{2} + b\,\sin(2\pi s)\right), \tag{93}$$

and

$$\mathbf{u}(\mathbf{x},0) = 0. \tag{94}$$

corresponding to a tubular membrane with elliptical cross section in a stationary fluid. For completeness, we set the following parameters

$$\mu = 1,\ \ \rho = 1,\ \text{ and } \sigma = 10000. \tag{95}$$

Because the chosen spring constant σ is stiff, the dynamics occur over a small time scale ($t \leq 0.04$) and require a small time step to resolve.

Figure 20 presents the velocity field and evolution of the system at the first time step and $t = 0.0010, 0.0015, 0.0020, 0.0035, 0.0045$ when the boundary

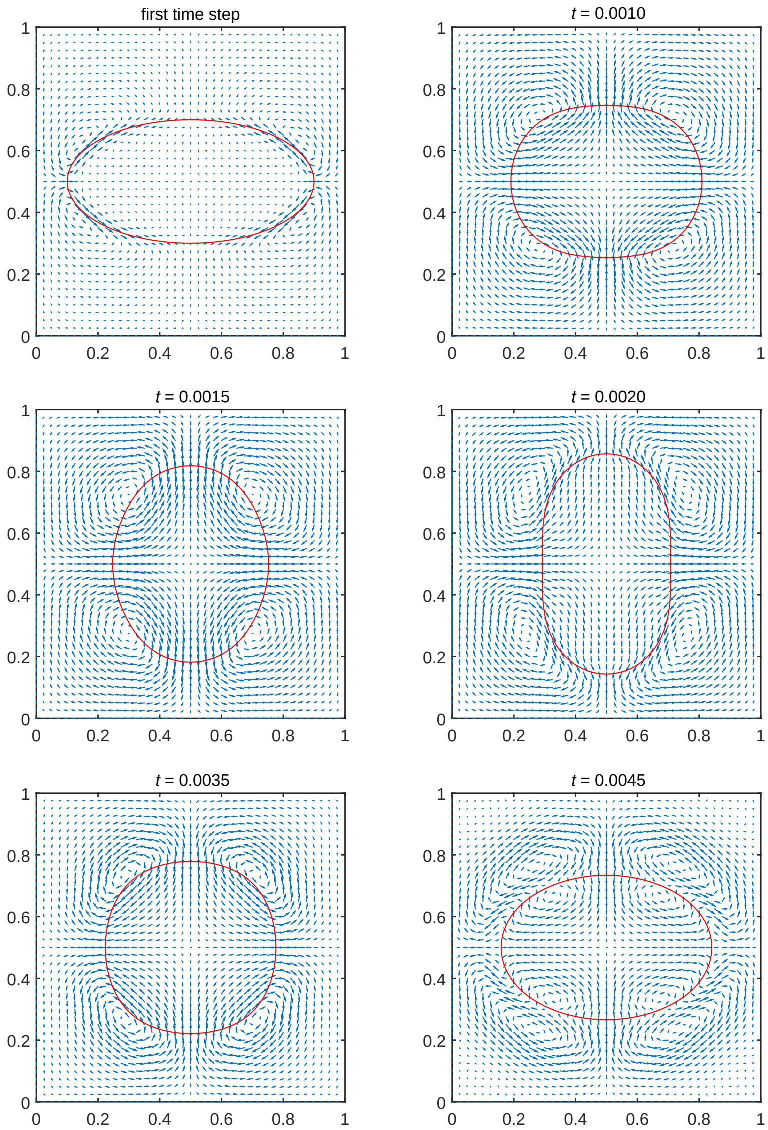

Figure 20: Tubular membrane, $\sigma = 10000$, $n_x = n_y = 40$, $n_b = 120$, and $\Delta t = 5 \times 10^{-5}$: Velocity field and profiles of the membrane at different times.

speed and flow are relatively large. It is shown that the restoring movement of the membrane boundary induces an oscillating flow with vortices at the diagonal corners. The results are consistent with those of [44, 45, 46].

Because the membrane is closed and the fluid is incompressible, the volume inside the oscillating membrane remains constant. By plotting the maximum and minimum radii of the membrane in time, shown in Figure 21, we verify that the approximate solution converges to the correct steady state. The results are in good agreement with those presented in [45].

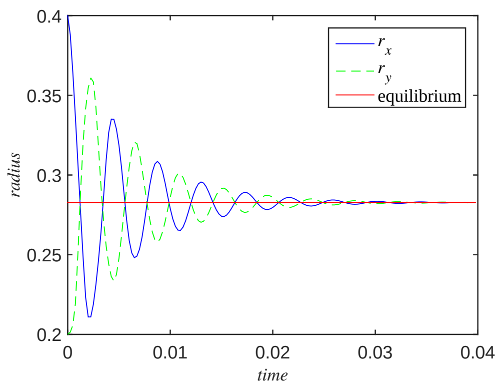

Figure 21: Tubular membrane, $\sigma = 10000$, $n_x = n_y = 80$, $n_b = 240$, and $\Delta t = 1 \times 10^{-5}$: Evolution of r_x and r_y. The cross section oscillates as it converges to the equilibrium state.

The area (or "volume") of fluid inside the membrane can be effectively used as a measure of the numerical error. It is well known that immersed boundary computations can suffer from poor area conservation, which becomes significant during extreme flow condition such as that we are considering here with large σ. Where appropriate, the combined compact IRBF results are compared with those of the central FDM reported in [37, 40] in which the authors implemented the FDM with various time-stepping discretisation schemes, Runge-Kutta (RK), forward Euler/backward Euler (FE/BE), Crank-Nicholson (CN), and midpoint (MP). Table 5 presents an analysis to study the conservation of the enclosed area. It could be seen that the present numerical errors are very small, less than $1.1929E-01\%$, and they are much smaller than those obtained by the FDM.

In Figure 22, we plot the u- and v-velocity profiles along the horizontal and vertical centrelines, respectively, at $t = 0.02$ for different grid sizes. The parameters used are described in Table 5. It is seen that the present solution approaches its convergent state with a fast rate as the grid size and time step are decreased. The velocity profiles are consistent with those results reported in the literature.

Figure 23 presents the pressure distribution at different times. It can be seen that the contractive boundary force generates an abrupt pressure jump inside and outside the membrane. These plots are in good agreement with those reported in the literature.

In order to make further comparison with FDM results obtained in [37, 40], we particularly increase the spring constant to $\sigma = 100000$. Table 6 shows that present combined compact IRBF produces much smaller area losses than those obtained by the FDM.

To evaluate the effects of the regularised delta function, which is first/second-order accurate, on the overall accuracy, a grid convergence study for this problem is carried out. Results concerning velocities on three different grids, $[40 \times 40, 80 \times 80, 160 \times 160]$, are compared with those on a fine grid of $[320 \times 320]$. Parameters used are $\sigma = 10000$, $\Delta t = 2 \times 10^{-6}$, an ellipse with

Table 5: Tubular membrane, $\sigma = 10000$, and $t = 0.020$: The conservation of the area enclosed by the membrane. The "area loss" is computed relative to the exact area. The area A is numerically computed using the instantaneous membrane profile.

Method	Parameters			Computed area	Exact area	Area loss
	$n_x \times n_y$	n_b	Δt	A	A_e	%
present combined compact IRBF	20×20	60	1×10^{-4}	0.2506400	0.2513274	2.7350E-01
present combined compact IRBF	40×40	120	5×10^{-5}	0.2510325	0.2513274	1.1733E-01
present combined compact IRBF	60×60	180	2×10^{-5}	0.2511366	0.2513274	7.5940E-02
present combined compact IRBF	80×80	240	1×10^{-5}	0.2511915	0.2513274	5.4095E-02
present combined compact IRBF	100×100	300	1×10^{-5}	0.2512219	0.2513274	4.1998E-02
present combined compact IRBF	120×120	360	5×10^{-6}	0.2512397	0.2513274	3.4913E-02
present combined compact IRBF	140×140	420	2×10^{-6}	0.2512522	0.2513274	2.9923E-02
FDM-RK1 [40]	64×64	192	1.3×10^{-5} (max)	—	0.2513274	2.8
FDM-RK4 [40]	64×64	192	8.0×10^{-5} (max)	—	0.2513274	2.4
FDM-FE/BE [40]	64×64	192	7.0×10^{-5} (max)	—	0.2513274	4.4
FDM-CN [37]	64×64	192	6.0×10^{-5} (max)	—	0.2513274	7.6
FDM-MP [40]	64×64	192	8.0×10^{-5} (max)	—	0.2513274	8.4
FDM-MP [40]	64×64	192	1.6×10^{-4} (max)	—	0.2513274	13.1

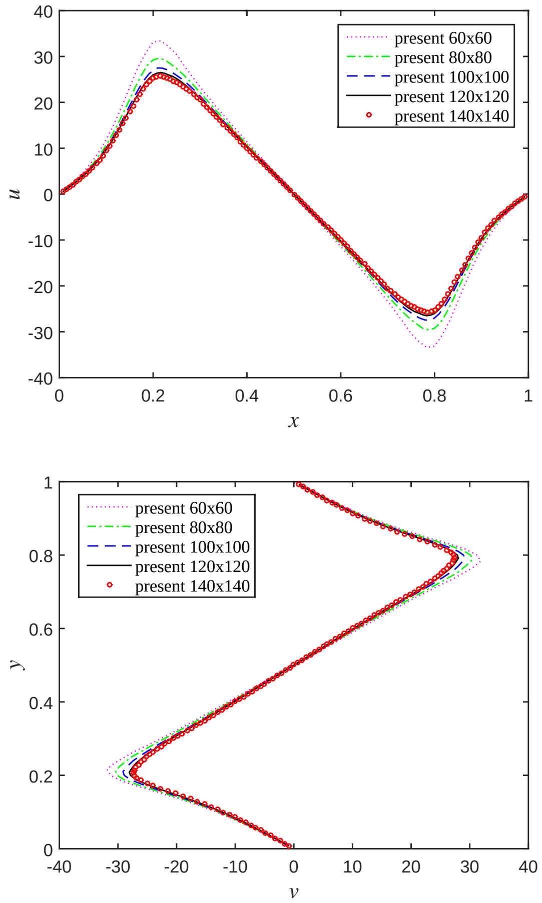

Figure 22: Tubular membrane, $\sigma = 10000$, and $t = 0.01$: Profiles of the u-velocity along the horizontal centreline (top) and the v-velocity along the vertical centreline (bottom). It is noted that the curves for the last two grids are almost indistinguishable, which shows that the solution converges at the grid of 120×120.

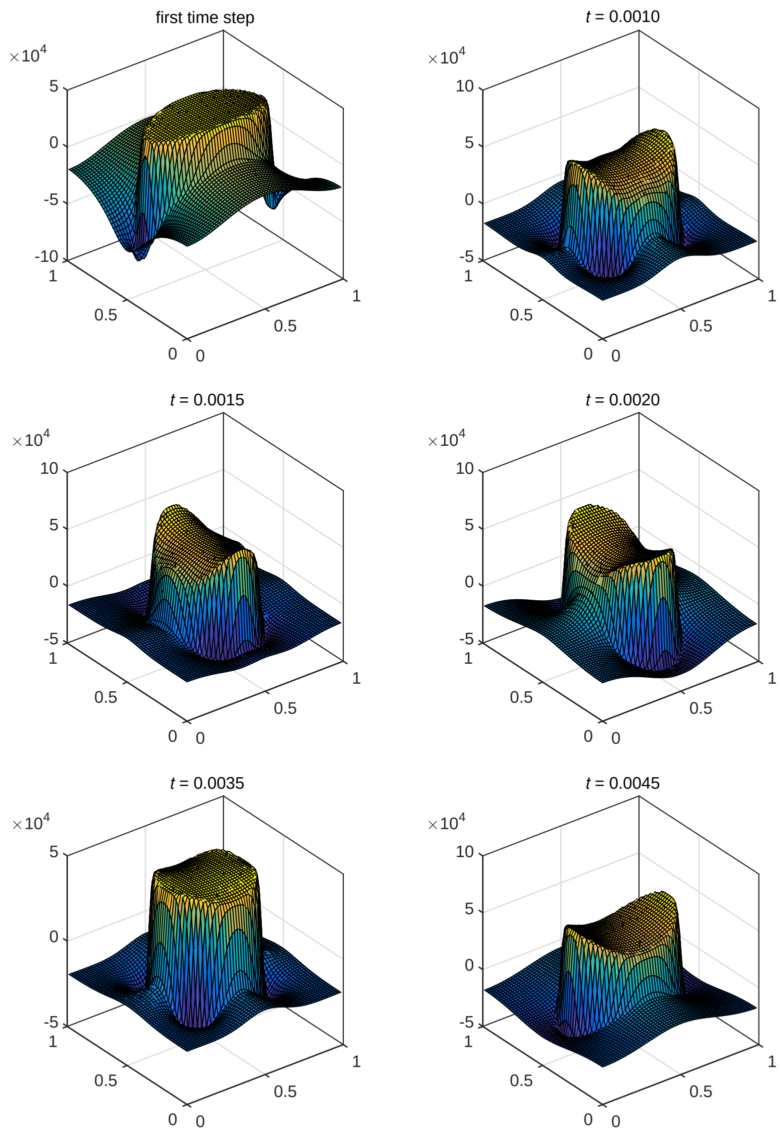

Figure 23: Tubular membrane, $\sigma = 10000$, $n_x = n_y = 60$, $n_b = 180$, $\Delta t = 2 \times 10^{-5}$: Pressure distribution at different times.

Table 6: Tubular membrane, $\sigma = 100000$, and $t = 0.005$: The conservation of the area enclosed by the membrane. The "area loss" is computed relative to the exact area. The area A is numerically computed using the instantaneous membrane profile.

Method	Parameters			Computed area	Exact area	Area loss
	$n_x \times n_y$	n_b	Δt	A	A_e	%
present combined compact IRBF	20×20	60	5×10^{-5}	0.2506783	0.2513274	2.5829E-01
present combined compact IRBF	40×40	120	2×10^{-5}	0.2510409	0.2513274	1.1399E-01
present combined compact IRBF	60×60	180	1×10^{-5}	0.2510734	0.2513274	1.0108E-01
present combined compact IRBF	80×80	240	5×10^{-6}	0.2511273	0.2513274	7.9614E-02
present combined compact IRBF	120×120	360	2×10^{-6}	0.2511778	0.2513274	5.9510E-02
present combined compact IRBF	140×140	420	1×10^{-6}	0.2511921	0.2513274	5.3846E-02
FDM-RK1 [40]	64×64	192	1.0×10^{-6} (max)	—	0.2513274	4.4
FDM-RK4 [40]	64×64	192	3.0×10^{-5} (max)	—	0.2513274	4.4
FDM-FE/BE [40]	64×64	192	1.0×10^{-5} (max)	—	0.2513274	5.2
FDM-CN [37]	64×64	192	1.0×10^{-5} (max)	—	0.2513274	6.8
FDM-MP [40]	64×64	192	2.5×10^{-5} (max)	—	0.2513274	6.8
FDM-MP [40]	64×64	192	5.0×10^{-5} (max)	—	0.2513274	11.9

major axis of 0.75 and minor axis of 0.5 and a flow domain of $[0, 2] \times [0, 2]$. The present results and those obtained by the second-order accurate FDM [39] are shown in Table 7. It can be seen that similar rates are obtained; however, for all grids employed, the present solution is about one and two orders of magnitude better than the FDM one. It is expected that improved rates of the proposed method can be acquired if a fixed smooth function [26] is employed to replace the delta function.

Table 7: Tubular membrane, $t = 0$: Velocity errors versus the grid refinement.

present combined compact IRBF				
$n_x \times n_y$	$L_\infty(u)$	Local rate$^{(*)}$	$L_\infty(v)$	Local rate$^{(*)}$
40×40	5.7921E-04	—	1.0641E-04	—
80×80	1.9506E-04	1.57	4.2909E-05	1.31
160×160	6.0462E-05	1.69	1.3957E-05	1.62
FDM [39]				
$n_x \times n_y$	$L_\infty(u)$	Local rate$^{(*)}$	$L_\infty(v)$	Local rate$^{(*)}$
40×40	1.0170E-02	—	5.0540E-03	—
80×80	4.4694E-03	1.19	2.0512E-03	1.30
160×160	1.5012E-03	1.57	7.4032E-04	1.47

$^{(*)}$Local rate=-log$[error_{new}/error_{old}]$/log$[n_{xnew}/n_{xold}]$.

6. Concluding Remarks

In this paper, we have successfully implemented the combined compact IRBF scheme along with the fully coupled velocity-pressure approach for simulating fluid flow problems and with the IBM for FSI simulations in the Cartesian-grid point-collocation structure. Computational results of fluid flow problems indicate that the present scheme is superior to the standard

FDM, HOC, compact IRBF, and coupled compact IRBF schemes in terms of the solution accuracy and the convergence rate with the grid refinement. It is shown that the present scheme achieves up to eight-order accuracy when simulating the fluid flow problems. Numerical results of immersed fibre/membrane FSI problems show that although the order of accuracy of the present scheme is generally similar to FDM approaches reported in the literature, the present approach is nonetheless more accurate than FDM approaches at comparable grid spacings. Very good results are obtained using relatively coarse grids. In this work, the essence of the combined compact IRBF, fully coupled and IBM methods are outlined; and, the high-order solution accuracy, better decay rate, and better volume conservation features are demonstrated. It is believed that the combined compact IRBF approximation primarily contributes to achieving significant improvements in the solution accuracy.

Acknowledgements

The first author would like to thank USQ for an International Postgraduate Research Scholarship. The authors would like to thank the reviewers for their helpful comments.

[1] S. K. Chakrabarti, Numerical Models in Fluid-Structure Interaction, Advances in Fluid Mechanics, Vol. 42, WIT Press, Ashurst Lodge, Ashurst, Southampton, SO40 7AA, 2005.

[2] E. H. Dowell, K. C. Hall, Modeling of fluid-structure interaction, Annual Review of Fluid Mechanics 33 (2001) 445-490. doi:10.1146/annurev.fluid.33.1.445.

[3] H. J. P. Morand, R. Ohayon, Fluid-Structure Interaction: Applied Numerical Methods, Wiley, 111 River Street, Hoboken, NJ 07030-5774, 1995. doi:10.1002/zamm.19960760705.

[4] G. Hou, J.Wang, A. Layton, Numerical methods for fluid-structure interaction - A review, Community Computational Physics 12 (2) (2012) 337-377. doi:10.4208/cicp.291210.290411s.

[5] C. S. Peskin, Numerical analysis of blood flow in the heart, Journal of Computational Physics 25 (3) (1997) 220-252. doi:10.1016/0021-9991(77)90100-0.

[6] D. M. McQueen, C. S. Peskin, E. L. Yellin, Fluid dynamics of the mitral valve: physiological aspects of a mathematical model, American Journal of Physiology-Heart & Circulatory Physiology 242 (6) (1982) H1095-H1110.

[7] L. A. Miller, C. S. Peskin, When vortices stick: an aerodynamic transition in tiny insect flight, Journal of Experimental Biology 207 (17) (2004) 3073-3088. doi:10.1242/jeb.01138.

[8] L. J. Fauci, C. S. Peskin, A computational model of aquatic animal locomotion, Journal of Computational Physics 77 (1) (1988) 85-108. doi:10.1016/0021-9991(88)90158-1.

[9] R. Dillon, L. Fauci, A. Fogelson, D. G. III, Modeling biofilm processes using the immersed boundary method, Journal of Computational Physics 129 (1) (1996) 57-73. doi:10.1006/jcph.1996.0233.

[10] G. Iaccarino, G. Kalitzin, P. Moin, B. Khalighi, Local grid refinement for an immersed boundary RANS solver, AIAA paper 586 (2004). doi:10.2514/6.2004-586.

[11] R. Mittal, G. Iaccarino, Immersed boundary methods, Annual Review of Fluid Mechanics 37 (2005) 239-261. doi:10.1146/annurev.fluid.37.061903.175743.

[12] F. Sotiropoulos and X. Yang, Immersed boundary methods for simulating fluid-structure interaction, Progress in Aerospace Sciences 65 (2014) 1-21. doi:10.1016/j.paerosci.2013.09.003.

[13] Benchmark spectral results on the lid-driven cavity flow, Computers & Fluids 27 (4) (1998) 421-433. doi:10.1016/S0045-7930(98)00002-4.

[14] S. K. Lele, Compact finite difference schemes with spectral-like resolution, Journal of Computational Physics 103 (1) (1992) 16-42. doi:10.1016/0021-9991(92)90324-r.

[15] Z. Tian, X. Liang, P. Yu, A higher order compact finite difference algorithm for solving the incompressible Navier-Stokes equations, International Journal for Numerical Methods in Engineering 88 (6) (2011) 511-532. doi:10.1002/nme.3184.

[16] H. Fadel, M. Agouzoul, P. K. Jimack, High-order finite difference schemes for incompressible flows, International Journal for Numerical Methods in Fluids 65 (9) (2011) 1050-1070. doi:10.1002/fld.2228.

[17] E. J. Kansa, Multiquadrics-A scattered data approximation scheme with applications to computational fluid-dynamics-I. Surface approximations

and partial derivative estimates, Computers & Mathematics with Applications 19 (8-9) (1990) 127-145. doi:10.1016/0898-1221(90)90270-T.

[18] E. J. Kansa, Multiquadrics-A scattered data approximation scheme with applications to computational fluid-dynamics-II. Solutions to parabolic, hyperbolic and elliptic partial differential equations, Computers & Mathematics with Applications 19 (8-9) (1990) 147-161. doi:10.1016/0898-1221(90)90271-K.

[19] G. E. Fasshauer, Meshfree approximation methods with Matlab, World Scientific Publishing, 5 Toh Tuck Link, Singapore 596224, 2007.

[20] D. Ngo-Cong, N. Mai-Duy, W. Karunasena, T. Tran-Cong, A numerical procedure based on 1D-IRBFN and local MLS-1D-IRBFN methods for fluid-structure interaction analysis, Computer Modeling in Engineering & Sciences 83 (5) (2012) 459-498. doi:10.3970/cmes.2011.083.459.

[21] N. Thai-Quang, N. Mai-Duy, C. D. Tran, T. Tran-Cong, High-order alternating direction implicit method based on compact integrated-RBF approximations for unsteady/steady convection-diffusion equations, Computer Modeling in Engineering & Sciences 89 (3) (2012) 189-220. doi:10.3970/cmes.2012.089.189.

[22] N. Mai-Duy, T. Tran-Cong, A compact five-point stencil based on integrated RBFs for 2D second-order differential problems, Journal of Computational Physics 235 (2013) 302-321. doi:10.1016/j.jcp.2012.10.048.

[23] C. M. T. Tien, N. Thai-Quang, N. Mai-Duy, C. D. Tran, T. Tran-Cong, A three-point coupled compact integrated RBF scheme for second-order

differential problems, Computer Modeling in Engineering & Sciences 104 (6) (2015) 425-469. doi:10.3970/cmes.2015.104.425.

[24] C. M. T. Tien, N. Thai-Quang, N. Mai-Duy, C. D. Tran, T. Tran-Cong, High-order fully coupled scheme based on compact integrated RBF approximation for viscous flows in regular and irregular domains, Computer Modeling in Engineering & Sciences 105 (4) (2015) 301-340. doi:10.3970/cmes.2015.105.301.

[25] C. M. T. Tien, N. Mai-Duy, C. D. Tran, T. Tran-Cong, A numerical study of compact approximations based on flat integrated radial basis functions for second-order differential equations, Computer & Mathematics with Applications (under review).

[26] M. C. Lai, C. S. Peskin, An immersed boundary method with formal second-order accuracy and reduced numerical viscosity, Journal of Computational Physics 160 (2) (2000) 705-719. doi:0.1006/jcph.2000.6483.

[27] D. F. Brittany, W. Jeffrey, MatIB user guide, Massachusetts Institute of Technology - Cambridge (accessed the URL on 3rd November 2015). URL https://github.com/eldila/MatIB

[28] N. Mai-Duy, Solving high order ordinary differential equations with radial basis function networks, International Journal for Numerical Methods in Engineering 62 (6) (2005) 824-852. doi:10.1002/nme.1220.

[29] I. A. Hassanien, A. A. Salama, H. A. Hosham, Fourth-order finite difference method for solving Burgers' equation, Applied Mathematics and Computation 170 (2005) 781-800. doi:10.1016/j.amc.2004.12.052.

[30] B. J. Noye, H. H. Tan, Finite difference methods for solving the two-dimensional advection-diffusion equation, International Journal for Numerical Methods in Fluids 9 (1) (1989) 75-98. doi:/10.1002/fld.1650090107.

[31] U. Ghia, K. N. Ghia, C. T. Shin, High-resolutions for incompressible flows using Navier-Stokes equations and a multigrid method, Journal of Computational Physics 48 (1982) 387-411. doi:10.1016/0021-9991(82)90058-4.

[32] P. M. Gresho, S. T. Chan, R. L. Lee, C. D. Upson, A modified finite element method for solving the time-dependent, incompressible Navier-Stokes equations. Part 2: Applications, International Journal for Numerical Methods in Fluids 4 (1984) 619-640. doi:10.1002/fld.1650040608.

[33] C. H. Bruneau, C. Jouron, An efficient scheme for solving steady incompressible Navier-Stokes equations, Journal of Computational Physics 89 (1990) 389-413. doi:10.1016/0021-9991(90)90149-U.

[34] G. B. Deng, J. Piquet, P. Queutey, M. Visonneau, Incompressible-flow calculations with a consistent physical interpolation finite-volume approach, Computers & Fluids 23 (8) (1994) 1029-1047. doi:10.1016/0045-7930(94)90003-5.

[35] M. Sahin, R. G. Owens, A novel fully implicit finite volume method applied to the lid-driven cavity problem - Part I: High reynolds number flow calculations, International Journal for Numerical Methods in Fluids 42 (1) (2003) 57-77. doi:10.1002/fld.442.

[36] N. Thai-Quang, K. Le-Cao, N. Mai-Duy, T. Tran-Cong, A high-order compact local integrated-RBF scheme for steady-state incompressible viscous flows in the primitive variables, Computer Modeling in Engineering & Sciences 84 (6) (2012) 528-557. doi:10.3970/cmes.2012.084.528.

[37] J. M. Stockie, Analysis and computation of immersed boundaries, with application to pulp fibres, Ph.D. thesis, The University of British Columbia (1997).

[38] Z. X. Gong, H. X. Huang, C. J. Lu, Stability analysis of the immersed boundary method for a two-dimensional membrane with bending rigidity, Communications in Computational Physics 3 (3) (2008) 704-723.

[39] R. J. Leveque, Z. Li, Immersed interface methods for Stokes flow with elastic boundaries or surface tension, SIAM Journal on Scientific Computing 18 (3) (1997) 709-735. doi:10.1137/S1064827595282532.

[40] J. M. Stockie, B. R.Wetton, Analysis of stiffness in the immersed boundary method and implications for time-stepping schemes, Journal of Computational Physics 154 (1) (1999) 41-64. doi:10.1006/jcph.1999.6297.

[41] L. Lee, R. J. Leveque, An immersed interface method for incompressible Navier-Stokes equations, SIAM Journal on Scientific Computing 25 (3) (2003) 832-856. doi:10.1137/S1064827502414060.

[42] D. V. Le, An immersed interface method for solving viscous incompressible flows involving rigid and flexible boundaries, Ph.D. thesis, Singapore-MIT Alliance (2005).

[43] E. P. Newren, Enhancing the immersed boundary method: stability, volume conservation, and implicit solvers, Ph.D. thesis, The University of Utah (2007).

[44] Y. G. Cheng, H. Zhang, Immersed boundary method and lattice Boltzmann method coupled FSI simulation of mitral leaflet flow, Computers & Fluids 39 (5) (2010) 871-881. doi:10.1016/j.compfluid.2010.01.003.

[45] K. W. Jeffrey, Immersed boundary method for shared-memory architectures (accessed the URL on 3rd November 2015). URL http://www.cs.usask.ca/faculty/spiteri/students/jwiens.pdf

[46] B. E. Griffith, On the volume conservation of the immersed boundary method, Communications in Computational Physics 12 (2) (2012) 401-432. doi:10.4208/cicp.120111.300911s.